Non-microglial downregulation of *PLCG2* impairs synaptic function and elicits Alzheimer disease-related hallmarks

Audrey Coulon[1,*], Florian Rabiller[1,*], Mari Takalo[2,*], Avishek Roy[3,*], Alexandre Pelletier[4,*], Henna Martiskainen[2,*], Dolores Siedlecki-Wullich[1], Nina Lannette-Weimann[1], Naďa Majerníková[1], Arthur Grenon[5], Vance Gao[1], Anaël Erhardt[3], Anne Pernodet[1], Morgane Lemaire[1], Floriane Limoge[1], Pauline Walle[1], Tiago Mendes[1], Karine Guyot[1], Célia Lemeu[1], Lukas-Iohan Carvalho[1], Ana Raquel Melo de Farias[1], Marc Hulsman[6-8], Chloé Najdek[1], Alejandra Freire-Regatillo[1], Orthis Saha[1], Philippe Amouyel[1], Camille Charbonnier[9], Jean-François Deleuze[10], Orio Dols-Icardo[11,12], Heli Jeskanen[2], Roosa-Maria Willman[2], Teemu Kuulasmaa[2], Mitja Kurki[13], John Hardy[14], Sami Heikkinen[2], Henne Holstege[6-8], Petra Mäkinen[2], Gaël Nicolas[15], Simon Mead[16], Michael Wagner[17,18], Alfredo Ramirez[17-21], Tuomas Rauramaa[22], Aarno Palotie[12], Rebecca Sims[23], Hilkka Soininen[24], John van Swieten[25], Julie Williams[26], Céline Bellenguez[1], Carla Gelle[1], Erwan Lambert[1], Marcos R. Costa[1,27,28,], Julia TCW[4,29], Enrico Glaab[30], Anne-Marie Ayral[1], Florie Demiautte[1], Benjamin Grenier-Boley[1], Manon Muntaner[1], Delphine Eberlé[5], Séverine Deforges[3], Joel Haas[5], Devrim Kilinc[1], Christophe Mulle[3,**], Julien Chapuis[1,**], Mikko Hiltunen[2,**], Julie Dumont[1,**,#], Jean-Charles Lambert[1,**,#]

[1] Univ. Lille, Inserm, CHU Lille, Institut Pasteur de Lille, U1167 - RID-AGE - Facteurs de risque et déterminants moléculaires des maladies liées au vieillissement, Lille, France
[2] Institute of Biomedicine, University of Eastern Finland, Kuopio, Finland
[3] Interdisciplinary Institute for Neuroscience, CNRS UMR 5297, University of Bordeaux, Bordeaux, France
[4] Department of Pharmacology, Physiology & Biophysics, Boston University Chobanian & Avedisian School of Medicine, Boston, MA 02118, USA
[5] Univ. Lille, Inserm, CHU Lille, Institut Pasteur de Lille, U1011- EGID, F-59000 Lille, France
[6] Genomics of Neurodegenerative Diseases and Aging, Human Genetics, Vrije Universiteit Amsterdam, Amsterdam UMC location VUmc, Amsterdam, the Netherlands
[7] Alzheimer Center Amsterdam, Neurology, Vrije Universiteit Amsterdam, Amsterdam UMC location VUmc, Amsterdam, the Netherlands
[8] Amsterdam Neuroscience, Neurodegeneration, Amsterdam, the Netherlands
[9] Univ Rouen Normandie, Inserm U1245 and CHU Rouen, Department of Biostatistics and CNRMAJ, F-76000 Rouen, France
[10] Commissariat à L'Énergie Atomique et Aux Énergies Alternatives, Centre National de Recherche en Génomique Humaine, Université Paris-Saclay, Gif-sur-Yvette, France
[11] Department of Neurology, II B Sant Pau, Hospital de la Santa Creu i Sant Pau, Universitat Autònoma de Barcelona, Barcelona, Spain
[12] Biomedical Research Networking Center on Neurodegenerative Diseases, National Institute of Health Carlos III, Madrid, Spain
[13] Institute for Molecular Medicine Finland, University of Helsinki, Helsinki, Finland
[14] Reta Lila Weston Research Laboratories, Department of Molecular Neuroscience, University College London Institute of Neurology, London, UK
[15] Univ Rouen Normandie, Inserm U1245 and CHU Rouen, Department of Genetics and CNRMAJ, F-76000 Rouen, France
[16] Medical Research Council Prion Unit at University College London, University College London Institute of Prion Diseases, London, UK
[17] Department of Cognitive Disorders and Old Age Psychiatry, University Hospital Bonn, Medical Faculty, Bonn, Germany
[18] German Center for Neurodegenerative Diseases, Bonn, Germany

[19] Division of Neurogenetics and Molecular Psychiatry, Department of Psychiatry and Psychotherapy, Faculty of Medicine and University Hospital Cologne, University of Cologne, Cologne, Germany
[20] Department of Psychiatry and Glenn Biggs Institute for Alzheimer's and Neurodegenerative Diseases, San Antonio, TX, USA
[21] Cologne Excellence Cluster on Cellular Stress Responses in Aging-Associated Disease (CECAD), University of Cologne, Cologne, Germany
[22] Department of Pathology, Kuopio University Hospital, Kuopio, Finland and Unit of Pathology, Institute of Clinical Medicine, University of Eastern Finland, Kuopio, Finland
[23] Medical Research Council Centre for Neuropsychiatric Genetics and Genomics, Division of Psychological Medicine and Clinical Neuroscience, School of Medicine, Cardiff University, Cardiff, UK
[24] Department of Neurology, University of Eastern Finland, Kuopio, Finland
[25] Department of Neurology, Erasmus Medical Centre, Rotterdam, the Netherlands
[26] UK Dementia Research Institute and Moondance Dementia Research Laboratory, Dept Psychological Med., Cardiff University.
[27] Roche Pharma Research and Early Development, Neuroscience and Rare Diseases, Roche Innovation Center Basel, F. Hoffmann-La Roche Ltd., Basel, Switzerland
[28] Brain Institute, Federal University of Rio Grande do Norte, Natal, Brazil
[29] Bioinformatics Program, Faculty of Computing & Data Sciences, Boston University, Boston, MA 02215, USA
[30] Luxembourg Centre for Systems Biomedicine, University of Luxembourg, Esch-sur-Alzette, Luxembourg

* Contributed equally as co-first author
** Contributed equally as co-last author
[#] Address correspondence to: julie.dumont@univ-lille.fr, jean-charles.lambert@pasteur-lille.fr

ABSTRACT

We developed a high content screening to investigate how Alzheimer disease (AD) genetic risk factors may affect synaptic mechanisms in rat primary neuronal cultures. Out of the target genes identified, we found that *Plcg2* downregulation in mouse dentate gyrus neurons consistently disrupted dendritic morphology and synaptic function. In human neuronal cultures (hNCs), *PLCG2* downregulation also impaired synaptic function and increased Aβ levels and Tau phosphorylation. Very rare *PLCG2* loss-of-function (LoF) variants were associated with a 10-fold increased AD risk. *PLCG2* LoF carriers exhibit low mRNA/protein *PLCG2/*PLCγ2 levels and the R953* LoF mutation compromised synaptic function and increased AD hallmarks in hNCs. Single nuclei RNAseq analyses confirmed that the downregulation of *PLCG2* impacted pathways related to synaptic and neuronal functions, potentially through neurexin in neurons. In conclusion, PLCγ2 downregulation could increase AD risk by impairing synaptic functions and increasing the Aβ levels and Tau phosphorylation in neurons.

Key words: Alzheimer's disease, *PLCG2*, synapse, high-content screening, patch-clamp, iPSCs, GSK3β, Tau, microelectrode arrays

INTRODUCTION

Alzheimer's disease (AD) is characterized by intracellular aggregation of abnormally hyperphosphorylated Tau protein and extracellular accumulation of amyloid-beta (Aβ) in plaques. According to the "amyloid cascade hypothesis", Aβ aggregation is an early toxic condition that can induce Tau aggregation and neuronal death. However, while recent clinical studies using anti-Aβ immunotherapies in principle support this hypothesis[1], it has been regularly revised to reflect the advancements in our understanding of AD[2–4]. It is now well accepted that the amyloid cascade hypothesis appears to be over-simplistic and fails to account for the intricacy and heterogeneity of the pathophysiological processes involved in the common forms of the disease.

Since the proportion of risk attributable to genetic susceptibility factors for AD has been estimated to be between 60% and 80% in twin studies[5], defining the AD genetic component should help in better understanding the pathophysiological processes and in generating complementary or alternative hypotheses. The development of genome-wide association studies (GWAS) and high-throughput sequencing has considerably advanced the AD genetic landscape over the last fifteen years, leading to the characterization of 76 loci associated with the AD risk[6–8]. Based on this new genetic landscape of AD, and beyond inflammation processes[9], we proposed synaptic fragility/sensitivity as a pathological trigger[10], depending on genetic risk factors, some of which have already been linked to synaptic mechanisms, such as *BIN1*, *FERMT2*, *PTK2B* or *CD2AP*[9–12]. This notion fits with key clinical observations suggesting that synapse dysfunction/loss is (i) one of the earliest pathological hallmarks in the brain and (ii) the strongest marker of cognitive decline[13–15]. Within this background, we systematically addressed the potential implication of the genes located in the loci associated with AD risk (as reported in[6]) in synaptic mechanisms. For this purpose, we developed a high-content screening (HCS) approach to systematically analyze the impact of the downregulation of a large number of AD risk genes on synaptic density and to further explore the potential implication of these genes in synaptic function.

RESULTS

HCS identifies GWAS-defined genes as potential modulators of synapse density

We developed an HCS approach to systematically characterize the effect on synaptic density of 198 genes located in the 76 loci associated with AD risk and selected as being expressed in brain cells (according to publicly available RNAseq datasets, see Methods online). A lentiviral shRNA library targeting these 198 genes was developed. The screen was performed in 384-well plates using rat hippocampal primary neuronal cultures (PNCs) transduced at day 1 in vitro (DIV1) using two multiplicities of infection (MOI 2 and 4, **Fig. 1a,b**). Immunocytochemistry was conducted at DIV21 against Synaptophysin 1 (Syp), Homer1 (Hom1) and Map2, pre-synaptic, post-synaptic and somatodendritic markers, respectively (**Fig. 1c,d**; supplementary. Fig. S1a)[16]. Synaptic density was then assessed *via* a high-content analysis workflow by assigning each post-synaptic structure to the nearest pre-synaptic structure, as previously described[17]. Non-targeting shRNA (shNT) and shRNA against Syp (shSyp) were used as controls. The complete HCS results are presented in supplementary Table S1. We selected AD risk genes with the strongest effect on synaptic density (top and bottom 2.5%) in three independent experiments, resulting in five genes (*Usp6nl*, *Psmc3*, *Plcg2*, *Csnk1g1*, *Cyb561*) associated with lower synaptic density and four genes (*Snx1*, *Ica1l*, *Oplah* and *Nck2*) associated with higher synaptic density when downregulated (**Fig. 1c**). For these nine genes, we confirmed the impact of shRNA-mediated downregulation on protein levels in PNCs (supplementary Fig. S1b, c). In conclusion,

our HCS approach allowed us to identify several genes located within the loci associated with AD risk that strongly modulate synaptic density in rat PNCs.

Plcg2 impacts electrophysiological properties of PNCs

We first determined whether proteins encoded by the nine selected genes could be detected in synaptosomes purified from PNCs (**Fig. 1e, f**). Except for Cyb561 (data not shown), we detected their presence in the PSD95 and/or non-PSD95 fractions. We then analyzed the impact of their downregulation on the electrophysiological properties of mature PNCs (at DIV21) using multielectrode arrays (MEAs). As a positive control, the downregulation of *Syp* significantly decreased burst frequency, a read-out for neuronal activity (**Fig. 1g**). Similarly, the downregulation of *Usp6nl* and *Plcg2* significantly decreased burst frequency whereas the opposite was observed upon *Oplah* downregulation. Of note, *Usp6nl* downregulation also significantly impacted mean spike frequency (supplementary. Fig. S1d). We further focused on *Plcg2* as this AD risk gene was believed to be almost exclusively expressed in microglia and, as a consequence, it has been extensively investigated in this cell type[18–21]. However, *PLCG2* is also expressed in glutamatergic neurons as evidenced in publicly available single nuclei RNA sequencing (sn-RNA seq) datasets from human brain[22,23] (supplementary Fig. S2) and therefore merits further investigation of its possible role in synaptic function in the context of AD pathogenesis.

Plcg2 downregulation in the mouse dentate gyrus reduces dendritic arborization complexity and spine density of granule cells

Plcg2/PLCG2 is expressed in the mouse and human dentate gyrus (DG)[24], which is the main gateway from the entorhinal cortex to the hippocampus. Synaptic plasticity in the DG is strongly affected in mouse models of AD[25,26]. Lentiviral vectors encoding either a shRNA against *Plcg2* (LV-shPLCG2) or a non-targeting control shRNA (LV-shNT), combined with GFP were injected into the dorsal hippocampus of adult mice of both sexes in the ipsi- (LV-shPLCG2) and contra-lateral (LV-shNT) hemispheres, respectively (**Fig. 2a** and supplementary Fig. S3a, b). We stained brain sections with an antibody against IBA1, a marker for microglia cells (supplementary Fig. S3c) and found that the number of GFP expressing cells positive for IBA1 was negligible (for both LV-shPLCG2 and LV-shNT vectors), indicating that microglial cells were not transduced by the lentiviral vectors. Analysis of GFP fluorescence images of DG neurons from shNT (n=35 neurons) and shPLCG2 (n=42 neurons) injected mice (**Fig. 2b**) revealed that *Plcg2* downregulation resulted in a reduction in dendritic length (shNT = 148±12 µm *vs* shPLCG2 = 77±9 µm, $p<0.001$; **Fig. 2c**) and dendritic volume (shNT = 270±32 μm^3 *vs* shPLCG2 = 87±5 μm^3, $p<0.001$; **Fig. 2d**), but not in the complexity index ($p=0.24$) or total branch number ($p=0.52$; **Fig. 2e, f**). We observed a decrease in the number of intersections in a Sholl analysis ($p<0.0001$, intersection *vs* distance from soma $F_{(24, 1560)}=23.23$; **Fig. 2g, h**), in the spine density (number of spines per µm: shNT = 0.70±0.04, n=73 neurites *vs* shPLCG2 = 0.27±0.01, n=75 neurites, $p<0.0001$; **Fig. 2i**) and alterations in the morphology of dendritic spines in shPLCG2-transduced DG granule cells, with decreased spine length (shNT = 0.73±0.06 µm, n=89 *vs* shPLCG2 = 0.53±0.05 µm, n=101, $p<0.0001$) and head diameter (shNT = 0.48±0.02 µm, n=100 *vs* shPLCG2 = 0.29±0.01 µm, n=103, $p<0.0001$; **Fig. 2j, k**). Overall, in congruence with our findings *in vitro*, *Plcg2* downregulation markedly impairs dendritic morphology and spine density in DG granule cells *in situ*.

Plcg2 downregulation in the mouse dentate gyrus impairs electrophysiological properties of granule cells

We then prepared slices for the electrophysiological recording of DG granule cells transduced with shPLCG2 or shNT as visualized by their GFP fluorescence (**Fig. 3a**). We assessed the intrinsic electrophysiological properties (shNT, n=15 cells; shPLCG2, n=13 cells; **Fig. 3b, c** and supplementary Fig. S4a,b). *Plcg2* downregulation did not change the resting membrane potential (RMP) (shNT = –57.2±2.2 mV *vs* shPLCG2 = –62.4±2.2 mV, p=0.11; **Fig. 3d**), but led to a reduction in the input resistance (shNT = 570±79 MOhm *vs* shPLCG2 = 312±35 MOhm, p=0.0061; **Fig. 3e**), which was accompanied by an increase in the half-width of action potentials (shNT = 1.17 ms *vs* shPLCG2 = 1.25 ms, p=0.027, supplementary Fig. S4c,d). We found that the amount of current required for the cell to fire an action potential (the rheobase) was significantly higher following *Plcg2* downregulation (shNT = –57±11 pA *vs* shPLCG2 = –86±10 pA, p=0.022; **Fig. 3f**). The number of spikes triggered by depolarizing pulses as a function of the amplitude of current injected also showed that shPLCG2-transduced DG neurons were less excitable ($F_{(1,\ 588)}$ = 10.87, df=1, p=0.001, ordinary 2-way ANOVA; **Fig. 3g**). Overall, *Plcg2* downregulation leads to a substantial decrease in input resistance and in neuronal excitability. It can be suggested that Plcg2 contributes to the regulation of voltage-dependent ion channels around resting membrane potential of DG granule cells. We then performed voltage-clamp recordings in the presence of tetrodotoxin (TTX; 500 nM) to assess the impact of *Plcg2* downregulation on spontaneous miniature excitatory post-synaptic currents (mEPSCs) (**Fig. 3h**). We found significant differences in the average frequency of mEPSCs between shNT (n=27) and shPLCG2 (n=15) transduced neurons (shNT = 0.47±0.07 Hz *vs* shPLCG2 = 0.27±0.08 Hz, p=0.026; **Fig. 3i**). This result is consistent with the observed reduction of spine density, albeit to a lesser extent (–43% for mEPSC frequency *vs* –61% for spine density), which might be due to a compensatory increase in spontaneous release at the remaining synapses. In addition, *Plcg2* downregulation resulted in a decrease in the amplitude of mEPSCs (shNT = 13.6±0.7 pA *vs* shPLCG2 = 10.8±0.5 pA, p=0.034; cumulative distribution of mEPSC amplitudes, p=0.0008; **Fig. 3j, k**). We have finally recorded EPSCs evoked by the electrical stimulation of the perforant path in the presence of bicuculline to block GABA-A receptors (**Fig. 3l**). We measured the amplitude of AMPA-EPSCs (at –70 mV; **Fig. 3m**) and NMDA-EPSCs (at +40 mV in the presence of NBQX; **Fig. 3n**) and found that the NMDA/AMPA-EPSC ratio was largely reduced following *Plcg2* downregulation (shNT = 1.15, n=12 *vs* shPLCG2 = 0.31, n=13, p=0.019; **Fig. 3o**). Our data suggest that the downregulation of Plcg2 selectively decreases the amount of post-synaptic NMDARs at synapses in DG cells. In conclusion, in accordance with our results *in vitro*, *Plcg2* downregulation markedly impairs electrophysiological properties of DG granule cells.

Downregulation of *PLCG2* in human neuronal cultures negatively impacts synaptic density and function

We then sought to extend our findings in rodents to an *in vitro* model of human neurons, derived from human induced pluripotent stem cells (iPSCs, ASE-9109 cell line[27]). After 4 weeks of spontaneous differentiation from neural progenitor cells transduced with either shNT or shPLCG2, we obtained a mixed culture of mature human induced neurons and astrocytes, which we will refer to as human neuronal cultures (shNT-hNCs or shPLCG2-hNCs; **Fig. 4a**). We validated *via* immunoblotting that PLCγ2 downregulation in this mixed culture was specific as it did not impact PLCγ1 expression (**Fig. 4b**). To characterize the impact of *PLCG2* downregulation on synaptic density in hNCs, we used custom microfluidic devices in which mature neuronal synapses can be fluidically isolated in a distinct (synaptic) chamber and easily quantified. As in the case of HCS, we performed immunocytochemistry against synaptic markers and assessed synaptic density using a previously described algorithm[17] (**Fig. 4c**). We fully replicated in hNCs the results obtained in the HCS experiments using rat NPCs, *i.e.*, *PLCG2*

221 downregulation decreased synaptic density (**Fig. 4c,d**). Similar results were obtained when using rat
222 PNCs cultured in microfluidic devices (supplementary Fig. S5). Lastly, we analyzed the impact of *PLCG2*
223 downregulation on the electrophysiological properties of hNCs using MEAs. Again, we replicated in
224 hNCs the results we obtained in rat PNCs, *i.e.*, *PLCG2* downregulation induced a significant decrease in
225 burst frequency, and a downward trend was observed for mean spike frequency (p=0.052; **Fig. 4e**). In
226 conclusion and in accordance with our results observed in the rodent brain, *PLCG2* downregulation
227 impacts synaptic density and function *in vitro* in hNCs.
228
229 **Downregulation of *PLCG2* in human neuronal cultures increases both Tau phosphorylation and the**
230 **levels of Aβ**
231 We next tested the potential impact of *PLCG2* downregulation in hNCs on the different hallmarks of
232 AD, *i.e.*, amyloid precursor protein (APP) metabolism and quantity/phosphorylation state of Tau. In
233 shPLCG2-hNCs, a significant increase in both APP (**Fig. 4f,g**) and Aβ levels (**Fig. 4h**) was detected. *PLCG2*
234 downregulation was also associated with a strong increase in Tau phosphorylation at multiple epitopes
235 (**Fig. 4f,i**). Of note, an increase in total Tau protein levels was also detected (**Fig. 4f,g**). We finally
236 investigated whether the impact of *PLCG2* downregulation on Tau hyperphosphorylation could be
237 mediated by the regulation of ERK1/2, GSK3β, p38 MAPK or AKT kinases, known regulators of Tau
238 phosphorylation (**Fig. 4j,k)**. No difference in the total protein levels or phosphorylation statuses of
239 ERK1/2 or p38 MAPK was observed when *PLCG2* was downregulated. However, *PLCG2* downregulation
240 increased the level of phosphorylated GSK3β at Y216 and decreased the level of phosphorylated AKT
241 at S473 (**Fig. 4k**). Both epitope sites are indicative of the active forms of these kinases. Altogether,
242 these data indicate that *PLCG2* downregulation is associated with increased Aβ levels and Tau
243 phosphorylation, the latter potentially *via* the AKT/GSK3β axis.
244 To confirm that the effect of *PLCG2* downregulation on AD hallmarks was specific, we performed
245 rescue experiments by overexpressing PLCG2 in shPLCG2-hNCs. Remarkably, rescuing PLCγ2 levels
246 almost completely restored Aβ levels, as well as total Tau and Tau phosphorylation levels (**Extended**
247 **Fig. 1a-d**). Finally, the changes in GSK3β and AKT phosphorylation levels were also restored after
248 overexpressing PLCG2 (**Extended Fig. 1a,e,f**). In conclusion, restoring PLCG2 expression in shPLCG2-
249 hNCs can reverse the changes in components of AD hallmarks.
250
251 **Rare *PLCG2* loss-of-function variants are associated with an increase in AD risk**
252 Importantly, our above-mentioned data suggest that the *PLCG2* downregulation may be deleterious
253 and favor the development of AD through synaptic impairment and increased Aβ levels and Tau
254 hyperphosphorylation. Therefore, we postulated that loss-of-function (LoF) variants responsible for a
255 univocal reduction in *PLCG2/*PLCγ2 expression/activity might be associated with an increase in AD risk.
256 To address this possibility, we used two independent whole exome sequencing (WES) datasets. In a
257 Finnish sample of 527 AD cases (ADGEN) and 8,707 controls (see Material and Methods), the
258 comparison of allele number between AD patients (2 carriers) and controls (3 carriers) indicated an
259 overrepresentation of LoF variants in AD cases (OR = 11.0, 95% CI = 1.8-66.3; Pearson's χ^2 test,
260 p=0.0009; Fisher's exact test, p=0.03). In the ADES dataset (including 8,732 AD cases and 8,955 controls
261 from Germany, France, Spain, the Netherlands and the United Kingdom[7]), the comparison of LoF allele
262 number between AD patient (9 carriers) and control (1 carrier) groups also indicated an
263 overrepresentation in AD cases (OR = 9.2, 95% CI = 1.2-72.9; Pearson's χ^2 test, p=0.01; Fisher's exact
264 test, p=0.01). Finally, a meta-analysis was performed, which, in turn, indicated that the *PLCG2* LoF

265 variants increase the risk of AD (OR = 9.7, 95% CI = 2.0-47.7, p=0.005; **Fig. 5a** and supplementary Table
266 S2 for a full description of the LoF variants).
267
268 **Effects of *PLCG2* LoF variants on AD pathological markers and on *PLCG2*/PLCγ2 levels**
269 We next analyzed a post-mortem sample obtained from the temporal cortex of an AD patient carrying
270 the *PLCG2* LoF p.R953* variant to see whether partial loss-of-function of PLCγ2 influences AD-related
271 neuropathology. The patient who was a female was previously diagnosed as clinical AD and was
272 classified as a Braak stage VI case according to neurofibrillary pathology in the neuropathological
273 examination. Quantification of AD-related pathological hallmarks in the brain and CSF of this patient
274 did not show any major alterations with respect to four Braak stage-matched AD patient samples
275 (supplementary Table S3 and supplementary Fig. S6). Even if a large variation was observed between
276 individuals for PLCγ2 levels in brain lysates, the PLCγ2 level was on average 70% lower in the *PLCG2*
277 p.R953* variant carrier as compared to other AD cases (**Fig. 5b,c**). We did not detect additional specific
278 bands for the p.R953* variant below the full-length PLCγ2. In addition, we had access to RNA extracted
279 from the frozen blood sample of an ADGEN AD patient carrying the *PLCG2* p.Q816* variant. We
280 randomly selected four age-matched AD patients without *PLCG2* LoF variants from the ADGEN cohort.
281 RNA analysis of these samples revealed on average a 40% reduction in the mRNA levels of *PLCG2* in
282 the p.Q816* variant sample as compared to the other AD samples (**Fig. 5d**). These findings collectively
283 support the involvement of nonsense-mediated mRNA decay (NMD), as both mutations introduce
284 premature termination codons (PTCs) that meet the established criteria for triggering this pathway[28].
285 However, a detailed analysis of the RNA sequencing data revealed that the Q816* T allele—
286 corresponding to the premature stop codon—was not entirely eliminated by the NMD machinery, as
287 it was still present in 20% of the total PLCG2 reads (data not shown). These results suggest that both
288 LoF variants, *PLCG2* p.Q816* and *PLCG2* p.R953*, likely trigger NMD, leading to reduced mRNA and
289 protein levels of *PLCG2*/PLCγ2.
290
291 **The *PLCG2* p.R953* LoF variant impairs synaptic function and increases both Tau phosphorylation**
292 **and Aβ levels**
293 We generated iPSCs carrying the *PLCG2* p.R953* LoF variant using CRISPR/Cas9 editing (KOLF 1.2J line,
294 see Methods online; **Fig 5e** and supplementary Fig. S7). In *PLCG2*^{R953*}-hNCs, we observed reduced
295 PLCγ2 protein levels when compared to *PLCG2*^{WT}-hNCs (**Fig 5f, g)**, supporting NMD due to the p.R953*
296 PTC. As reported in shPLCG2-hNCs, we observed that the *PLCG2* p.R953* variant associated with (i) a
297 significant decrease in synaptic density (**Fig 5h,i**); (ii) a significant decrease in burst frequency along
298 with a trend toward reduced mean spike frequency (p=0.061; **Fig. 5j**); (iii) a significant increase in total
299 Tau levels and in Tau phosphorylation at T231 (**Fig. 5k-m**); (iv) a significant increase in Aβ levels in
300 conditioned media (**Fig 5n**); and (v) a significant increase in GSK3β phosphorylation at Y216 (**Fig 5o,p)**.
301 No significant decrease in AKT phosphorylation at S473 was observed, although a similar trend was
302 noted (–45%, p=0.057). Altogether, these data indicate that the *PLCG2* p.R953* LoF variant mirrors the
303 phenotypic alterations previously observed following shRNA-mediated downregulation of PLCG2.
304
305 **Single nuclei (sn)-RNAseq analyses confirm that lower *PLCG2* expression affects synaptic pathways**
306 To analyze PLCG2-dependent signaling pathways in neurons and astrocytes derived from human iPSCs
307 independently, we conducted single-nucleus RNA sequencing (sn-RNAseq) in shPLCG2-hNCs *vs* shNT-
308 hNCs, and in *PLCG2*^{R953*}-hNCs *vs PLCG2*^{WT}-hNCs. After performing quality control (supplementary Fig.
309 S8) and clustering (**Fig. 6a** and supplementary Fig. S8), we observed a higher proportion of inhibitory

neurons in shPLCG2-hNCs (**Fig. 6b**), a change mirrored in *PLCG2*^{R953*}-hNCs to a lower extent. Differential expression analysis revealed a higher number of differentially expressed genes (DEGs) in shPLCG2-hNCs (**Fig. 6c**). This may be attributed to the more pronounced reduction in *PLCG2* expression as compared to the *PLCG2* R953-hNCs model, although model-specific factors are also likely to play a role, i.e., genetic background (ASE-9109 and KOLF2.1J), (ii) the mode of PLCG2 downregulation (shRNA-mediated knock-down versus an isogenic point mutation), and (iii) polyclonal versus monoclonal cell line. To disentangle the effects of reduced *PLCG2* expression from model-specific factors, we conducted separate functional enrichment analyses in each cellular model (supplementary Fig S9). Despite the models having different DEG distribution (**Fig 6c,** supplementary Tables S4 and S5), many enriched pathways overlapped, for instance those linked to synaptic function and neuronal development (**Fig. 6d, e**, and supplementary Table S6). Notably, about 25-45% of DEGs in *PLCG2*^{R953*}-hNCs overlapped with those in shPLCG2-hNCs, which supports a shared PLCG2-driven signature (**Fig. 6d**). Pathway analysis of these shared DEGs revealed consistent enrichment in synaptic organization, neuronal differentiation and the calcium signaling pathway (**Fig. 6e,** and supplementary Table S6).

As we observed an activation of GSK3β following *PLCG2* downregulation in our different models (**Extended fig. 1f**, **Fig. 4k**, **Fig. 5p**), we conducted regulon analyses by selecting several transcription factors that are known to depend on GSK3β activation (CREB, FOXO1, LEF1, NFATC2, NFKB, and TCF7L2)[29–33]. We found that several of these regulons were differentially represented in PLCG2-downregulated cells compared to WT cells, especially in excitatory and inhibitory neurons (supplementary Fig. S9i).

We also investigated intercellular communication using CellChat[34]. On average, 727 ligand–receptor (L/R) interactions were inferred *per* sample, grouped into 89 signaling pathways, with excitatory–inhibitory neuron interaction being strongest (supplementary Fig. S10b). Differential analysis revealed 18 and 10 altered L/R signaling pathways in shPLCG2-hNCs *vs* shNT-hNCs and *PLCG2*^{R953*}-hNCs *vs* *PLCG2*^{WT}-hNCs, respectively, with three main pathways depending on NRXN, ADGRL and PTPR, upregulated or downregulated in both models in neurons (**Fig. 6f,g** and supplementary Fig. S10). Among them, NRXN-dependent pathways were strongly upregulated in excitatory and inhibitory neurons across models (**Fig. 6g**). To strengthen the potential implication of neurexins, we selected NRXN3 for further validation, given that this isoform has been most consistently implicated in AD pathogenesis[35–39]. We observed a trend towards lower levels (–47%, p=0.076) of NRXN3 protein in PLCG2^{R953*}-hNCs compared to PLCG2^{WT}-hNCs (**Fig. 6h**), although NRXN3 mRNA levels were not different in neurons from PLCG2^{R953*}-hNCs compared to PLCG2^{WT}-hNCs (supplementary Table S4). This supports that NRXN3-dependent L/R signaling pathways are altered in our cellular models. To note, we also observed Laminin signaling downregulated in vascular leptomeningeal cells (VLMCs)–astrocytes communication, although less consistently (supplementary Fig S10c).

Finally, we sought to detect a potential AD-related transcriptomic signature in by comparing our sn-RNAseq results with publicly available snRNAseq databases and found a significant overlap in DEGs with the SEA-AD snRNAseq dataset[40], predominantly in excitatory neurons and, to a lesser extent, in inhibitory neurons (**Fig 6i**).

Altogether, these results suggest that *PLCG2* downregulation perturbs neuronal and synaptic functions, at least partly *via* neuron-neuron communication, with NRXN/ADGRL signaling emerging as a key candidate pathway. In addition, these observations suggest that PLCG2 downregulation can participate to generate, in part, an AD-related transcriptomic signature in excitatory neurons.

355 **DISCUSSION**
356
357 To determine if and how AD genetic risk factors contribute to synaptic failure, we developed an HCS
358 to systematically characterize the impact of the downregulation of GWAS-defined genes on synaptic
359 density. Among the genes with the strongest impact on synaptic density, *PLCG2* was one of the best
360 hits (despite the absence of microglia in our HCS). In AD, *PLCG2* has been mostly studied in microglia
361 and shown to be implicated in multiple microglia-related signaling pathways[18–21]. However, strong
362 evidence supports a role for PLCγ2 in synaptic function: (i) we and others found that *PLCG2* is also
363 expressed in neurons[22–24]; (ii) we observed that Plcγ2 is localized to both the pre- and post-synaptic
364 compartments; (iii) we demonstrated that PLCγ2 downregulation impacts synaptic density and
365 neuronal electrophysiological properties using four distinct experimental models (and different
366 shRNAs).
367 To further support the importance of PLCγ2 and its downregulation in AD pathophysiology, we
368 determined that very rare LoF variants in *PLCG2* are associated with an increased risk of AD in two
369 independent WES datasets. Two of these LoF variants, p.Q816* and p.R953* were associated with a
370 decrease in *PLCG2*/PLCγ2 expression in the blood or brain and we confirmed such a decrease in PLCγ2
371 expression in *PLCG2*^{R953*} hNCs. Remarkably, we also observed that the R953* variant leads to increased
372 Tau phosphorylation and Aβ levels, suggesting that PLCγ2 participates in the development of the two
373 main hallmarks of AD. The shRNA-mediated downregulation of *PLCG2* also has the same impact as the
374 variant, supporting the idea that a decrease in *PLCG2* activity is harmful. This is consistent with the fact
375 that the functionally hypermorphic *PLCG2* p.P522R variant is protective against AD[24]. Interestingly, a
376 recent study using the cross-bred 5xFAD; Plcγ2-P522R knock-in mice revealed that the hypermorphic
377 P522R variant improves impaired synaptic function as well as behavioral deficits observed in 5xFAD
378 mice[21]. Collectively, these observations suggest mechanisms where the sustained activity of PLCγ2
379 becomes instrumental when the risk of AD (protective *vs* deleterious) is considered not only in
380 microglia, but also in neurons.
381 Characterizing the potential mechanisms through which PLCγ2 influences key hallmarks of AD in hNCs
382 is of particular interest. We first focused on kinases known to be regulators of Tau phosphorylation.
383 Interestingly, our results suggest that GSK3β may play a role, among other factors, in mediating the
384 cellular response downstream of PLCγ2 downregulation. GSK3β is already known to be involved in the
385 regulation of APP metabolism, Tau phosphorylation and synaptic functions[41–43], making it a potential
386 link between PLCγ2 and the different phenotypes associated with its downregulation. Even though we
387 did not demonstrate that GSK3β is a direct intermediate of the PLCγ2 impact on AD hallmarks,
388 activation of GSK3β was fully abolished when PLCγ2 level was restored, supporting a specific impact of
389 PLCγ2 on this phenotype. Of note, neurons derived from iPSCs obtained from sporadic AD cases also
390 exhibit elevated Tau hyperphosphorylation, increased Aβ levels, and GSK3β activation[44]. AKT emerged
391 as a key target, as its membrane recruitment and activation depend on PLCγ2-regulated substrate
392 diacylglycerol (DAG). DAG-driven PKC activation can enhance AKT signaling and loss of PLCγ2 function
393 may thus reduce AKT activity, as observed. However, in the brains of Plcγ2-P522R knock-in mice,
394 Akt1/2 phosphorylation was reduced, casting doubt on this hypothesis[18].
395 We next performed snRNA-seq on both hNC models and found that numerous pathways related to
396 synaptic and neuronal functions were commonly affected. This is consistent with the observed
397 reductions in synaptic density and function following *PLCG2*/PLCγ2 downregulation. Notably, the
398 geneset "regulation of neuronal synaptic plasticity" was preferentially altered in excitatory neurons.
399 In addition, multiple pathways were impacted across different cell types, suggesting complex

intercellular interactions within hNC cultures. To investigate whether *PLCG2*/PLCγ2 downregulation preferentially disrupts interactions between specific cell populations, we performed a cell-cell communication analysis. This revealed that ADGRL and NRXN signaling were preferentially affected within neurons across both models. Both pathways are involved in synaptic function and psychiatric disorders[45–47]. NRXN signaling is of particular interest, as neurexins have been shown to regulate APP synaptic functions and/or modulate Aβ-induced synaptotoxicity[36,37,48].

Importantly, there are some limitations related to our cellular models that need to be mentioned. Firstly, *PLCG2* downregulation was associated with accelerated neuronal maturation in all models (see supplementary Fig. S9e). We thus cannot exclude that this difference in maturation impacts the observed modifications in phenotypes following *PLCG2* downregulation. However, it is worth noting that the downregulation of *Plcg2 in vivo*, which leads to profound changes in DG granule cell morphology and physiology, was performed in adult (>3 months old) mice, thus precluding a potential developmental effect that could be argued to explain part of the synaptic phenotype observed in rat PNCs and hNCs. Secondly, although the CellChat analyses and observation of enriched AD-related transcriptomic signatures in neurons both support the idea that *PLCG2* downregulation in neurons is responsible for the observed phenotypes, we cannot rule out the possibility that *PLCG2* downregulation in astrocytes contributes to them.

In conclusion, our results reveal a novel role for the AD genetic risk factor *PLCG2*. Downregulation of *PLCG2* specifically in neurons results in a signaling cascade that leads to the activation of GSK3β. This may promote increased Aβ secretion, Tau hyperphosphorylation, and synaptic dysfunction. These results are consistent with previous reports suggesting that PLCγ2 may modulate Tau pathology and disease progression in patients with mild cognitive impairment[49]. As an emerging major genetic risk factor for AD and other neurodegenerative diseases, *PLCG2* represents a promising therapeutic target. Future studies will be critical to delineate PLCγ2-dependent pathways in both microglia and neurons in order to identify relevant druggable targets.

Acknowledgement

The authors thank the BICeL platform of the Institut Biologie de Lille and the Vect'viral platform (INSERM US 005 – CNRS 3427 – TBMCore, Université de Bordeaux, France). The authors thank Karine Blary at the IEMN Lille for the microfabrication work. The authors also thank Sisko Juutinen, Eija Rahunen, and Minna Turunen for excellent technical support with immunohistochemistry. Fluorescent microscopy of human brain samples was carried out with the support of UEF Cell and Tissue Imaging Unit, University of Eastern Finland, Finland. This work has been funded by JPND (JPND2019-466-128, project PGM-AD; JPND2023-1822-030, project AD-PLCG2), ANR (GENSYNALZ, ANR-21-CE16-0010; AD-PLCG2, ANR-24-CE14-5376-01), COEN (grant number 6005), Alzheimer (grant number 903716), Fondation Claude Pompidou, Fondation pour la Recherche Médicale (ALZ201912009628), Fondation Recherche Alzheimer, Fondation Vaincre Alzheimer (grant number FR-22032), and the French RENATECH network (P-18-02737). This work was also supported by Lille Métropole Communauté Urbaine and the French government's LABEX DISTALZ program (Development of innovative strategies for a transdisciplinary approach to Alzheimer's disease), European Union under the European Regional Development Fund (ERDF), Hauts de France Regional Council (contract469 no.18006176), MEL (contract_18006176), and the French State (contract no. 2018-3-470 CTRL_IPL_Phase2). This work has been funded by Research Council of Finland (grant number 330178, 338182, 355604, 334802), the Sigrid Jusélius Foundation, Jane and Aatos Erkko Foundation, the Strategic Neuroscience Funding of the University of Eastern Finland, Faculty of Health Sciences of University of Eastern Finland and Alzheimer's Association (ADSF-24-1284326-C and AARG-22-926152). This work was also funded by ERC-StG Metabo3DC (101042759) to JTH et LabEx EGID (ANR 10-LABX-0046). This work was also supported by the National Institute of Health (R01AG082362, R01AG083941), Bright Focus Foundation, The Edward N. & Della L. Thome Memorial Foundation Awards Program in AD Research, Health Resources in Action. EG acknowledges support by the Luxembourg National Research Fund (INTER/JPND23/17999421/AD-PLCG2) and by the Luxembourg Fondation Wivine. This work is supported by the UK Dementia Research Institute [award number UKDRI-Car001] through UK DRI Ltd, principally funded by the Medical Research Council.

Author's Contribution

Conceptualization: J.C., J.D., J-C.L; **High content screening**: A.C., T.M., D.K., J.C., J-C.L.; **Cell culture experiments**: A.C., F.R., N.L-W., D.S-W., A.P., M.L., F.L., K.G., P.W., A.R.M.F., C.N., A. F-R., C.G., E.L., O.S., N.M., M.R.C., A-M.A, F.D., D.K., J.D.; **iPSCs QC**: N.L-W., B.G-B., M.M., J.D.; **Electrophysiological analyses**: A.R., A.E., S.D., C.M.; **Brain, blood and CSF analyses in human samples**: M.T., H.M., R.M.W., H.J., P.M., S.H., T.R., H.S., M.Hil.; **RNAseq analyses:** A.P., A.G., V.G., L-I.C., V.G., J.TCW., E.G., D.E., J.T.H; **WES sequencing data**: M.T., H.M., M.Hul., P.A., C.C., O.D-I., H.J., T.K., M.K., J.H., S.H., H.H., P.M., G.N., S.M., M.W., A.R., T.R., A.P., R.S., H.S., J.V.S., J.W., R.M.W., M.Hil., J-C.L.; **Genetic Analysis**: M.Hul., T.K., S.H., B.G-B., M.Hil., J-C.L. **Writing**: A.C., F.R., M.T., A.R., A.P., H.M., D.K., C.M., J.C., M.Hil., J.D., J-C.L.

Competing Interests Statement

All other authors declare no competing interests

Conflicts of interest

M.R.C. is an employee of Roche.

Availability of data and material

470 Cellular models used and/or analyzed in the current study are available from the corresponding
471 authors upon reasonable request. snRNA-seq and WGS datasets will be made available before
472 publication.

473 **Figure 1. High-content screening identified nine AD-associated genes that significantly impact**
474 **synaptic density and function in rat primary neuronal cultures**. **(a-b)** Impact of shRNA-mediated
475 downregulation of 198 AD-associated genes on synaptic density in rat hippocampal primary neuronal
476 cultures (PNCs), virally transduced at MOI 2 **(a)** and MOI 4 **(b)**. Data given as mean±SEM, n=3, top and
477 bottom 2.5% genes are shown in red. **(c)** Quantification of synapse density following the assignment
478 of Homer1 to Syp spots on Map2-positive dendrites. Data given as mean±SEM, n=3. **(d)** Representative
479 images of Map2, Syp and Homer1 immunostainings following shRNA-mediated downregulation of *Syp,*
480 *Psmc3, Plcg2, Cyb561, Snx1, Ica1l,* and *Nck2* at MOI 2; scale bar = 20 µm. **(e-f)** Immunoblotting **(e)** and
481 quantification **(f)** of PSD and non-PSD fractions in primary rat hippocampal neuron synaptosomes (at
482 DIV21) showing that Usp6nl, Psmc3, Plcγ2, Csnk1g1, Snx1, Ica1l, Oplah, and Nck2 proteins are
483 expressed in the PSD95 and/or non-PSD95 fractions. Data given as mean±SD. **(g)** Impact of shRNA-
484 mediated downregulation of *Syp, Usp6nl, Psmc3, Plcg2, Cyb561, Csnk1g1, Snx1, Ica1l, Oplah,* and *Nck2*
485 on the burst frequency in PNCs at DIV21, measured by MEA. Violin plots show median and quartile
486 lines, n=3. Statistical analyses were performed using Kruskal-Wallis test followed by Dunn's multiple
487 comparisons test. * $p<0.05$, *** $p<0.001$.
488
489 **Figure 2. *Plcg2* downregulation alters the morphology of DG granule cells**. **(a)** Schematic
490 representation of the experimental approach to downregulate *Plcg2* in the DG. The lentiviral
491 constructs were stereotaxically injected in either the ipsi- (LV-shPLCG2 for knock-down of *Plcg2*) or
492 contralateral (LV-shNT, control) hemispheres. **(b)** High magnification immunofluorescence images of
493 transduced DG cells as indicated by GFP expression, as well as a portion of dendritic branch with spines;
494 scale bars = 20 µm for left panels and 7 µm for right panels. **(c-f)** Measurements of dendritic length **(c)**,
495 dendritic volume **(d)**, complexity index **(e)**, and branch number **(f)** in transduced DG granule cells. **(g)**
496 Schematic diagram of the Sholl analysis, illustrating the morphological change in the dendritic tree of
497 representative control (grey) *vs* shPLCG2 (red) transduced DG granule cells. Scale bar = 20 µm. **(h)**
498 Distribution of intersections based on the Sholl analysis. **(i-k)** Measurements of average spine density
499 **(i)**, spine length **(j)** and spine head diameter **(k)**, indicating a marked alteration in synaptic contacts
500 onto DG granule cells. Data expressed as mean±SEM for bar graphs with individual data points. Sholl
501 statistical analysis (n ≥90 per condition) was performed using two-way ANOVA test. All other statistical
502 analyses were performed using Mann-Whitney test. * $p<0.05$, *** $p<0.001$, **** $p<0.0001$.
503
504 **Figure 3. *Plcg2* downregulation in DG granule cells decreases neuronal excitability and impacts**
505 **synaptic function. (a)** Representative image of maximum intensity projection of section labeled with
506 IBA1 (in magenta) and GFP (in green) showing the selective expression of viral vector in DG granule
507 cells. MolDG= molecular layer of DG, GrDG= granular DG, PoDG= polymorph layer of DG. Patch-clamp
508 recordings were performed from GFP expressing granule cells identified under the electrophysiology
509 microscope. Scale bar = 10 µm. **(b)** Representative traces from shNT (in grey) and shPLCG2 (in red)
510 transduced DG granule cells recorded in the current-clamp mode, with injection of current steps from
511 –80 pA to 0 pA with 10 pA increments. **(c)** Representative traces of current-clamp recordings showing
512 spike discharges triggered by a depolarization pulse of current (120 pA) from shNT (in grey) and
513 shPLCG2 (in red) transduced DG cells. **(d-f)** Current-clamp recordings were used to assess resting
514 membrane potential (RMP) **(d)**, input resistance **(e)** and rheobase **(f)**. **(g)** Number of spikes plotted
515 against current injected. **(h)** Representative traces of miniature excitatory post-synaptic currents
516 (mEPSCs) recorded in the voltage-clamp mode from shNT (in grey) and shPLCG2 (in red) DG cells in
517 presence of 500 nM TTX. **(i-k)** Measurements of average frequency of mEPSCs **(i),** average amplitude

518 of mEPSCs **(j)** and cumulative distribution of mEPSC amplitudes **(k)**. **(l)** Representative traces of AMPA-
519 EPSCs (at –70mV) and NMDA-EPSCs (at +40mV in the presence of 10 µM NBQX) evoked by the electrical
520 stimulation of the perforant path (at 0.1 Hz). **(m-o)**. Graphs representing the peak amplitude of AMPA-
521 EPSCs **(m)** and of NMDA-EPSCs **(n)**, and the ratio of NMDA-EPSCs *vs* AMPA-EPSCs **(o)** for each recorded
522 neuron. Data are represented as mean±SEM with bar and individual data points for average values. All
523 statistical analyses were performed using Mann-Whitney test with the exception of the cumulative
524 distribution where the Kolmogorov-Smirnov (KS) test was applied. * p<0.05, ** p<0.01, ***p<0.001.
525
526 **Figure 4. Downregulation of PLCγ2 in hNCs negatively impacts synapses and AD hallmarks. (a)**
527 Representative images of hNCs after 4 weeks of spontaneous differentiation from progenitors stably
528 expressing either a non-targeting shRNA (shNT) or a shRNA targeting *PLCG2* (shPLCG2); scale bar = 20
529 µm. **(b)** Western blots showing the specificity of PLCγ2 downregulation *via* shPLCG2 in hNCs. **(c)**
530 Immunofluorescence images of MAP2, SYP and HOMER1 synaptic markers in shNT- and shPLCG2-
531 transduced hNCs at 4 weeks; scale bar = 20 µm. **(d)** Synaptic marker densities for the two conditions.
532 Data given as mean±SEM **(e)** Impact of shPLCG2 on spike and burst frequencies in hNCs, measured *via*
533 MEA. Violin plots show median and quartile lines. **(f)** Representative Western blots of APP, total Tau
534 and Tau phosphorylated at T181, S202-T205, T217, T231 and S396-S404 in shNT- and shPLCG2-
535 transduced hNCs; **(g)** Quantification of APP and Tau levels for the two conditions. Data given as mean
536 ± SD, n=3. **(h)** Aβ peptides levels in shNT- or shPLCG2- transduced hNCs, measured by Alpha-LISA. Data
537 given as mean±SEM, n=3. **(i)** Tau phosphorylation levels in hNCs expressing (or not) shPLCG2. Data
538 given as mean±SD, n=3. **(j)** Representative Western blots of total and phosphorylated forms of ERK1/2,
539 GSK3β, P38-MAPK and AKT in shNT- and shPLCG2-transduced hNCs. **(k)** Quantification of total and
540 phosphorylated protein levels for these targets in shNT- and shPLCG2-transduced hNCs. Data given as
541 mean±SD, n=3. All statistical analyses were performed using Mann-Whitney test. *p<0.05, ***p<0.001.
542
543 **Figure 5. LoF nonsense variants increase AD risk and reduce *PLCG2*/PLCγ2 levels, consistently with**
544 **the detrimental impact of the LoF R953* mutation on synaptic function and AD hallmarks in hNCs.**
545 **(a)** Meta-analysis of the ADGEN and ADES Whole Exome Sequencing data. **(b)** Western blot of the post-
546 mortem brain tissue of an AD patient carrying the p.R953* variant in comparison with four other AD
547 cases. **(c)** Quantification of PLCγ2 protein levels in these samples. **(d)** RNAseq showing 40% decrease
548 in the blood *PLCG2* mRNA level in the p.Q816* carrier as compared to the mean of the matched control
549 group (n=4). **(e)** Representative images of hNCs after 4 weeks of spontaneous differentiation from
550 neural progenitors expressing either $PLCG2^{wt}$ or $PLCG2^{R953*}$; scale bar = 20 µm. (**f-g**) Representative
551 Western blot **(f)** and quantification **(g)** of PLCγ2 in $PLCG2^{wt}$ or $PLCG2^{R953*}$ hNCs at 4 weeks. **(h)**
552 Representative immunofluorescence images of MAP2, SYP and HOMER1 in $PLCG2^{wt}$ or $PLCG2^{R953*}$ hNCs
553 at 3 weeks; scale bar = 10 µm. **(i)** Synaptic marker densities for the two conditions. Data given as
554 mean±SEM; **(j)** Impact of the R953* mutation on spike and burst frequencies in hNCs, measured *via*
555 MEA. Violin plots show median and quartile lines, n=3; **(k)** Representative Western blots of APP, total
556 and T231-phospho-Tau, total and phospho-GSK3β, and total and phospho-AKT protein levels in
557 $PLCG2^{wt}$ and $PLCG2^{R953*}$ hNCs. Quantification of APP and Tau protein levels **(l)** and relative Tau
558 phosphorylation at T231 (**m**) in $PLCG2^{wt}$ or $PLCG2^{R953*}$ hNCs. Data given as mean±SD, n=4. **(n)** Aβ
559 peptides levels in the culture medium, measured *via* Alpha-LISA and normalized by total protein levels,
560 in $PLCG2^{wt}$ or $PLCG2^{R953*}$ hNCs. Data given as mean±SEM, n=4. Changes in total protein levels **(o)** and
561 relative phosphorylation **(p)** for GSK3β and AKT in in $PLCG2^{wt}$ or $PLCG2^{R953*}$ hNCs. Data given as
562 mean±SD, n=4. All statistical analyses were performed using Mann-Whitney test. *p<0.05.

563 **Figure 6. Sn-RNAseq analyses in shNT/shPLCG2 and PLCG2^{wt}/PLCG2^{R953*} hNCs. (a)** UMAP projection
564 of the different cell subpopulations identified in the 140,163 transcriptomically profiled high-quality
565 nuclei from 14 hNC cultures after QC (n=3 per group for shPLCG2 and shNT, and n=4 per group for
566 R953* and WT). **(b)** Mean proportion of cell types for each condition. (*: FDR<0.05, **: FDR<0.01, ***:
567 FDR<0.001, sccomp test[50], adjusted for the experimental batch. **(c)** Number of differentially expressed
568 genes (DEGs) comparing shPLCG2 *vs* shNT or R953* *vs* WT gene expression in each cell type. DEGs were
569 identified according to adjusted p-value<0.05 and |log2(FoldChange)|>0.5, using pseudobulk DESeq2
570 analysis, adjusted for average mitochondrial RNA percentage, library batch, and ambient RNA level. **(d)**
571 Common DEGs in the models, expressed as percent overlap of R953* *vs* WT DEGs with shPLCG2 *vs* shNT
572 DEGs for each cell type. Statistical significance was assessed using the hypergeometric test. **(e)**
573 Pathways enriched in the common DEGs between models. Representative pathways selected from the
574 top100 MSigDB CP and GO gene-sets enriched (FDR<0.05, hypergeometric test) in each cell type. **(f)**
575 Inferred incoming and outgoing interaction strength signaling difference comparing the two models
576 using CellChat with CellChatDB.human database excluding Non-protein Signaling. Difference of
577 cumulative interaction signaling received or sent by each cell type in the two models. **(g)** Ligand-
578 Receptors of ADGRL, NRXN and PTPR pathways differentially interacting (p-value<0.1, Wilcoxon rank-
579 sum test). **(h)** NRXN3 protein level in PLCG2^{wt} or PLCG2^{R953*} hNCs (n=3). Data given as mean±SD.
580 Statistical analysis was performed using Mann-Whitney test, p=0.076. **(i)** Overlap between DEGs found
581 when comparing PLCG2 downregulation models and DEGs reported for Dementia vs non-Dementia
582 groups in the SEA-AD postmortem brain snRNA-seq in two different brain regions. DLPFC: dorsolateral
583 prefrontal cortex; MTG: middle temporal gyrus. Over-representation analysis using hypergeometric test
584 using as background all genes tested for differential expression in the PLCG2 models.
585 Astro, astrocytes; Exc, excitatory neurons; Fib, fibroblasts; Inh, inhibitor neurons; NPCs,
586 neuroprogenitor cells; VLMC, vascular leptomeningeal cells.

587 **Extended Figure 1: PLCG2 re-expression in shPLCG2-hNCs reverse AD hallmark changes. (a)**
588 Representative Western blots of PLCγ2, APP, total and T231-phospho-Tau, total and phospho-GSK3β,
589 and total and phospho-AKT protein levels in shNT-hNCs, shPLCG2-hNCs, and shPLCG2-hNCs
590 overexpressing WT PLCG2 (shPLCG2-hNCs + PLCG2). **(b)** Quantification of APP and total Tau protein
591 levels in shNT-hNCs, shPLCG2-hNCs, and shPLCG2-hNCs + PLCG2. Data given as mean±SD, n=4. **(c)** Aβ
592 peptide levels in the culture medium, measured *via* Alpha-LISA and normalized by total protein levels,
593 in shNT-hNCs, shPLCG2-hNCs, and shPLCG2-hNCs + PLCG2. Data given as mean±SEM, n=4. **(d)**
594 Quantification of relative Tau phosphorylation at T231 in shNT-hNCs, shPLCG2-hNCs, and shPLCG2-
595 hNCs + PLCG2. Data given as mean±SD, n=4. **(e-f)** Changes in total protein levels **(e)** and relative
596 phosphorylation **(f)** of GSK3β and AKT in shNT-hNCs, shPLCG2-hNCs, and shPLCG2-hNCs + PLCγ2. Data
597 given as mean±SD, n=4. All statistical analyses were performed using Kruskal-Wallis test followed by
598 Dunn's multiple comparison test. *$p<0.05$.

REFERENCES

1. van Dyck, C. *et al.* Lecanemab in Early Alzheimer's Disease. *N. Engl. J. Med.* **388**, 142–143 (2023).
2. Herrup, K. The case for rejecting the amyloid cascade hypothesis. *Nat. Neurosci.* **18**, 794–799 (2015).
3. Selkoe, D. J. & Hardy, J. The amyloid hypothesis of Alzheimer's disease at 25 years. *EMBO Mol. Med.* **8**, 595–608 (2016).
4. Frisoni, G. B. *et al.* The probabilistic model of Alzheimer disease: the amyloid hypothesis revised. *Nat. Rev. Neurosci.* **23**, 53–66 (2022).
5. Gatz, M. *et al.* Role of Genes and Environments for Explaining Alzheimer Disease. *Arch. Gen. Psychiatry* **63**, 168 (2006).
6. Bellenguez, C. *et al.* New insights into the genetic etiology of Alzheimer's disease and related dementias. *Nat. Genet.* **54**, 412–436 (2022).
7. Holstege, H. *et al.* Exome sequencing identifies rare damaging variants in ATP8B4 and ABCA1 as risk factors for Alzheimer's disease. *Nat. Genet.* **54**, 1786–1794 (2022).
8. Lambert, J. C., Ramirez, A., Grenier-Boley, B. & Bellenguez, C. Step by step: towards a better understanding of the genetic architecture of Alzheimer's disease. *Mol. Psychiatry* **28**, 2716–2727 (2023).
9. Schürmann, B. *et al.* A novel role for the late-onset Alzheimer's disease (LOAD)-associated protein Bin1 in regulating postsynaptic trafficking and glutamatergic signaling. *Mol. Psychiatry* **25**, 2000–2016 (2020).
10. Eysert, F. *et al.* Alzheimer's genetic risk factor FERMT2 (Kindlin-2) controls axonal growth and synaptic plasticity in an APP-dependent manner. *Mol. Psychiatry* **26**, 5592–5607 (2021).
11. Giralt, A. *et al.* PTK2B/Pyk2 overexpression improves a mouse model of Alzheimer's disease. *Exp. Neurol.* **307**, 62–73 (2018).
12. Ojelade, S. A. *et al.* cindr, the Drosophila Homolog of the CD2AP Alzheimer's Disease Risk Gene, Is Required for Synaptic Transmission and Proteostasis. *Cell Rep.* **28**, 1799-1813.e5 (2019).
13. Masliah, E. Mechanisms of synaptic dysfunction in Alzheimer's disease. *Histol. Histopathol.* **10**, 509–519 (1995).
14. Barthet, G. & Mulle, C. Presynaptic failure in Alzheimer's disease. *Prog. Neurobiol.* **194**, 101801 (2020).
15. Ribarič, S. Detecting Early Cognitive Decline in Alzheimer's Disease with Brain Synaptic Structural and Functional Evaluation. *Biomedicines* **11**, 355 (2023).
16. Coulon, A. *et al.* High-Content Screening of Synaptic Density Modulators in Primary Neuronal Cultures. *Curr. Protoc.* **3**, e904 (2023).
17. Kilinc, D. *et al.* Pyk2 overexpression in postsynaptic neurons blocks amyloid β1-42-induced synaptotoxicity in microfluidic co-cultures. *Brain Commun.* **2**, fcaa139 (2020).
18. Takalo, M. *et al.* The Alzheimer's disease-associated protective Plcγ2-P522R variant promotes immune functions. *Mol. Neurodegener.* **15**, 1–14 (2020).
19. Claes, C. *et al.* The P522R protective variant of PLCG2 promotes the expression of antigen presentation genes by human microglia in an Alzheimer's disease mouse model. *Alzheimer's Dement.* **18**, 1765–1778 (2022).
20. Tsai, A. P. *et al.* PLCG2 is associated with the inflammatory response and is induced by amyloid plaques in Alzheimer's disease. *Genome Med.* **14**, 17 (2022).
21. Tsai, A. P. *et al.* Genetic variants of phospholipase C-γ2 alter the phenotype and function of microglia and confer differential risk for Alzheimer's disease. *Immunity* **56**, 2121-2136. (2023).
22. Li, Z. *et al.* APOE genotype determines cell-type-specific pathological landscape of Alzheimer's disease. *Neuron* **113**, 1380-1397. (2025).
23. Leng, K. *et al.* Molecular characterization of selectively vulnerable neurons in Alzheimer's disease. *Nat. Neurosci.* **24**, 276–287 (2021).
24. Magno, L. *et al.* Alzheimer's disease phospholipase C-gamma-2 (PLCG2) protective variant is a functional hypermorph. *Alzheimers. Res. Ther.* **11**, 16 (2019).

650 25. Jiang, N. *et al.* Impaired plasticity of intrinsic excitability in the dentate gyrus alters spike
651 transfer in a mouse model of Alzheimer's disease. *Neurobiol. Dis.* **154**, 105345 (2021).
652 26. Viana Da Silva, S. *et al.* Hippocampal Mossy Fibers Synapses in CA3 Pyramidal Cells Are Altered
653 at an Early Stage in a Mouse Model of Alzheimer's Disease. *J. Neurosci.* **39**, 4193–4205 (2019).
654 27. Saha, O. *et al.* The Alzheimer's disease risk gene BIN1 regulates activity-dependent gene
655 expression in human-induced glutamatergic neurons. *Mol. Psychiatry* **29**, 2634–2646 (2024).
656 28. Lejeune, F. Nonsense-Mediated mRNA Decay, a Finely Regulated Mechanism. *Biomedicines* **10**,
657 141 (2022).
658 29. Rekha, A. *et al.* GSK-3β dysregulation in aging: Implications for tau pathology and Alzheimer's
659 disease progression. *Mol. Cell. Neurosci.* **133**, 104005 (2025).
660 30. De Simone, A., Tumiatti, V., Andrisano, V. & Milelli, A. Glycogen Synthase Kinase 3β: A New Gold
661 Rush in Anti-Alzheimer's Disease Multitarget Drug Discovery? *J. Med. Chem.* **64**, 26–41 (2021).
662 31. Lauretti, E., Dincer, O. & Praticò, D. Glycogen synthase kinase-3 signaling in Alzheimer's disease.
663 *Biochim. Biophys. Acta Mol. Cell Res.* **1867**, 118664 (2020).
664 32. Huo, X. *et al.* GSK3 protein positively regulates type I insulin-like growth factor receptor through
665 forkhead transcription factors FOXO1/3/4. *J. Biol. Chem.* **289**, 24759–24770 (2014).
666 33. Inestrosa, N. C. & Varela-Nallar, L. Wnt signaling in the nervous system and in Alzheimer's
667 disease. *J. Mol. Cell Biol.* **6**, 64–74 (2014).
668 34. Jin, S., Plikus, M. V. & Nie, Q. CellChat for systematic analysis of cell–cell communication from
669 single-cell transcriptomics. *Nat. Protoc.* **20**, 180–219 (2025).
670 35. Martinez-Mir, A. *et al.* Genetic study of neurexin and neuroligin genes in Alzheimer's disease. *J.*
671 *Alzheimers. Dis.* **35**, 403–412 (2013).
672 36. Rahman, M. M., Westermark, G. T., Zetterberg, H., Härd, T. & Sandgren, M. Protofibrillar and
673 Fibrillar Amyloid-β Binding Proteins in Cerebrospinal Fluid. *J. Alzheimer's Dis.* **66**, 1053–1064
674 (2018).
675 37. Lee, A. K., Khaled, H., Chofflet, N. & Takahashi, H. Synaptic Organizers in Alzheimer's Disease: A
676 Classification Based on Amyloid-β Sensitivity. *Front. Cell. Neurosci.* **14**, 567721 (2020).
677 38. Hishimoto, A. *et al.* Neurexin 3 transmembrane and soluble isoform expression and splicing
678 haplotype are associated with neuron inflammasome and Alzheimer's disease. *Alzheimers. Res.*
679 *Ther.* **11**, 28 (2019).
680 39. Bot, N., Schweizer, C., Halima, S. Ben & Fraering, P. C. Processing of the synaptic cell adhesion
681 molecule neurexin-3beta by Alzheimer disease alpha- and gamma-secretases. *J. Biol. Chem.*
682 **286**, 2762–2773 (2011).
683 40. Gabitto, M. I. *et al.* Integrated multimodal cell atlas of Alzheimer's disease. *Nat. Neurosci.* **27**,
684 2366–2383 (2024).
685 41. Reddy, P. H. Amyloid beta-induced glycogen synthase kinase 3β phosphorylated VDAC1 in
686 Alzheimer's disease: implications for synaptic dysfunction and neuronal damage. *Biochim.*
687 *Biophys. Acta* **1832**, 1913–1921 (2013).
688 42. Hernandez, F., Lucas, J. J. & Avila, J. GSK3 and tau: two convergence points in Alzheimer's
689 disease. *J. Alzheimers. Dis.* **33 Suppl 1**, S141-4 (2013).
690 43. Ly, P. T. T. *et al.* Inhibition of GSK3β-mediated BACE1 expression reduces Alzheimer-associated
691 phenotypes. *J. Clin. Invest.* **123**, 224–235 (2013).
692 44. Ochalek, A. *et al.* Neurons derived from sporadic Alzheimer's disease iPSCs reveal elevated TAU
693 hyperphosphorylation, increased amyloid levels, and GSK3B activation. *Alzheimer's Res. Ther.*
694 **9**, 90 (2017).
695 45. Sita, L. V., Diniz, G. B., Horta, J. A. C., Casatti, C. A. & Bittencourt, J. C. Nomenclature and
696 comparative morphology of the teneurin/TCAP/ADGRL protein families. *Front. Neurosci.* **13**,
697 425 (2019).
698 46. Bourgeron, T. A synaptic trek to autism. *Curr. Opin. Neurobiol.* **19**, 231–234 (2009).
699 47. Vitobello, A. *et al.* ADGRL1 haploinsufficiency causes a variable spectrum of
700 neurodevelopmental disorders in humans and alters synaptic activity and behavior in a mouse
701 model. *Am. J. Hum. Genet.* **109**, 1436–1457 (2022).

48. Cvetkovska, V. *et al.* Neurexin-β Mediates the Synaptogenic Activity of Amyloid Precursor Protein. *J. Neurosci.* **42**, 8936–8947 (2022).
49. Kleineidam, L. *et al.* PLCG2 protective variant p.P522R modulates tau pathology and disease progression in patients with mild cognitive impairment. *Acta Neuropathol.* **139**, 1025–1044 (2020).
50. Mangiolaa, S. *et al.* Sccomp: Robust differential composition and variability analysis for single-cell data. *Proc. Natl. Acad. Sci. U. S. A.* **120**, e2203282120 (2023).

METHODS ONLINE

Primary neuronal culture

Primary hippocampal and cortical neurons were obtained from P0 Wistar rats, according to previously described procedures with minor modifications[51]. Culture media and supplements were from Gibco, ThermoFisher Scientific, unless mentioned otherwise. Briefly, hippocampi and cortex were isolated, washed with ice-cold dissection medium (HBSS supplemented with sodium pyruvate, HEPES, and penicillin/streptomycin), and trypsinized (2.5%) 10 min at 37°C. Trypsin was then inactivated with dissociation medium (MEM supplemented with inactivated FBS, Glutamax, D-glucose (Sigma), MEM vitamins, and penicillin/streptomycin) containing DNase (5 mg/ml, Sigma). Tissues were then dissociated in culture medium (Neurobasal A supplemented with glutamax and B27) to obtain a homogenous cell suspension, followed by centrifugation (200× g for 8 min). Cells were resuspended in the culture medium and seeded into plates that were pre-coated with poly-D-lysine (0.1 mg/mL, Sigma) in a borate buffer solution (0.31% boric acid and 0.475% sodium tetraborate, pH = 8.5). Cells were resuspended in culture medium and seeded in plates precoated with poly-D-lysine (0.1 mg/mL, Sigma) in borate buffer (0.31% boric acid, 0.475% sodium tetraborate, pH = 8.5) at a density of 50,000 cells/cm^2 for 384-well plates (Greiner bio-one), 100,000 cells/cm^2 for 24-well plates, 125,000 cells/cm^2 for 10 cm culture dishes or at 800,000 cells/cm^2 for microfluidics. For MEA 96-well plates, a 5 µL drop containing 15,000 cells was placed on the top of the electrodes, and medium was added after a minimum of 5 minutes to allow the cells to attach. For all types of culture, media was fully replaced after 24 h and cells were maintained in a tissue culture incubator at 37°C with 5% CO2 for 21 days.

Generation and quality control of the PLCG2 p.R953* KOLF2.1J hiPSC line.

Isogenic hiPSCs heterozygous for the p.R953* variant (R953*) were generated *via* CRISPR-Cas9 editing of the KOLF2.1J cell line[52] (wild-type, WT) by Applied StemCell (CA, USA). The guide RNA sequence was GAGCGGATTTCTCGGAAGTCAGG and the single-stranded oligodeoxyribonucleotide (ssODN) repair template sequence was GAAGTACTGATGACCTTTTTCTCTGTGTGCAGAAAATCATGACTTCTGAGAAATCCGCTCCTTTGTGGAGACGAA GGCTGACAGCATCATCAGACAGAAGCCCGTCGACCTCCTGAAGTACAATCAAAAGGGCCTGACCCGCGTCTACC CGAAGGGACAAAGAGTTGACTCTTCAAACTACGAGGGGTTCCGCCTCTGG. The successful introduction of the intended C>T heterozygous substitution (R953*) was verified using Sanger sequencing with the following primers: GTGGGAAAACTGGCGCTCCT and ACCATCTGGAACGCGACAG. The typical morphology of the CRISPR-edited iPSCs and the presence of pluripotency factors (e.g., OCT4 and SSEA4) were verified using live brightfield microscopy and immunofluorescence staining, respectively. Genomic DNA (gDNA) was extracted from the CRISPR-edited iPSCs and the parental KOLF2.1J iPSCs using NucleoSpin Tissue (Macherey-Nagel) according to the manufacturer's instructions. Fingerprinting of the cell lines was performed to rule out any mix-ups during the editing process or contamination by other cell lines. This was performed by assaying a microvariation at the human D1S80 locus on chromosome 1[53]. Allele variability between individuals was visualized by analyzing PCR products (primers: GTCTTGTTGGAGATGCACGTGCCCCTTGC and GAAACTGGCCTCCAAACACTGCCCGCCG) on 2% agarose gel. Potential off-target and on-target genomic alterations introduced by CRISPR editing were assessed using quantitative genomic PCR (qgPCR) as described previously[54] and whole-genome sequencing (WGS). qgPCR employed the following primers and probe: forward primer GTGGGAAAACTAGGCCCCTT, reverse primer ACCATCTGAGAACCGCACAG, and the fluorescently labeled probe 5' 6-FAM/CCGAGAAAT/ZEN/CCGCTCCTTTGTGGA/IBFQ 3' (PrimeTime Eco Probes, IDT), with Human TERT on

753 chromosome 5 serving as a reference gene (Human TaqMan Copy Number Reference Assays, Thermo
754 Fisher Scientific, cat. no. 4403316). Karyotypic integrity was confirmed by qPCR using the hPSC Genetic
755 Analysis kit (StemCell Technologies, cat. no. 07550) and WGS.
756 WGS of parental and edited KOLF2.1J lines was outsourced at Beijing Genomics Institute (BGI). Reads
757 were processed using the nf-core sarek pipeline (v3.5.1)[55], incorporating fastp (v0.24.0) for quality
758 control, dragmap (v1.2.1) for alignment to the reference genome GRCh38, and Picard MarkDuplicates
759 (v3.3.0) for duplicate marking. Variant calling was conducted with GATK HaplotypeCaller (v4.6.1.0),
760 chromosome copy number was estimated via tiddit (v6.6.1), and variants were annotated with
761 Ensembl's VEP (v111). Structural variant (SV) detection was conducted using three software: DELLY
762 (v1.7.2)[56], Manta (v1.6.0)[57], and Smoove (v0.2.8; https://github.com/brentp/smoove) coupled with
763 duphold (v0.2.3)[58]. Alignment of reads was performed by sarek using BWA (v0.7.18) instead of
764 dragmap as these three SV callers perform better with this aligner to detect discordant and split reads.
765 Joint calling was performed for each software using default parameters including both parental and
766 edited KOLF2.1J lines. Quality control was performed and SVs were retained only if they met the
767 following criteria: a quality score (QUAL) above 200, read coverage below 100, a minimum of five
768 supporting reads per allele and an allele balance between 0.2 and 0.8 for heterozygous calls. For
769 homozygous calls, at least ten supporting reads and an allele balance of 0.9 or higher were required.
770 Software-specific quality thresholds were also applied in DELLY (FILTER=PASS, excluding LowQual
771 genotypes), Manta (FILTER=PASS, genotypes classified as PASS or HomRef), and Smoove (GQ>20,
772 SHQ=4 for heterozygous calls, deletions with DHFFC<0.7, and duplications with DHFFC>1.25). Resulting
773 SVs from each tool were then merged using SURVIVOR (v1.0.7)[59], with a maximum allowed breakpoint
774 distance of 500 base pairs and considering both SV type and strand orientation. The final set of SVs
775 was restricted to those identified by all three tools (or by both DELLY and Manta in the case of
776 insertions, as Smoove does not detect this SV type) and only those whose genotype assignments
777 between software were consistent across software (i.e. heterozygous versus homozygous and non-
778 missing) were retained. Sample contamination was evaluated using VerifyBamID (v2.0.1). Default
779 parameters were applied for all pipeline steps.
780 WGS analyses confirmed the precise introduction of the intended C>T heterozygous substitution
781 (R953*) at chromosome 16, position 81,936,183 (GRCh38). Five additional single nucleotide variants
782 were detected within the *PLCG2* gene region (chr16:81,738,248–81,962,685). Two of them
783 (chr16:81,936,284:C>T and chr16:81,936,287:A>G) were homozygous and intentionally introduced as
784 synonymous mutations in the design to disrupt Cas9 target sites and prevent re-cutting post-ssODN
785 repair. The three other mutations (chr16:81,936,175:C>A, chr16:81,936,218 C>T, and chr16:81,919,070
786 A>T) were heterozygous mutations. The chr16:81,936,175:C>A is a missense variant (P950H) but this
787 mutation is in phase with the intended C>T heterozygous substitution we introduced (R953*); its
788 impact is therefore negligible. The chr16:81,936,218 C>T and chr16:81,919,070 A>T mutations are
789 unlikely to affect protein function since the first one is a synonymous variant and the second one is
790 located in an intron. Quality control confirmed normal ploidy and the absence of CRISPR-induced large
791 deletions, insertions, chromosomal rearrangements, or loss of heterozygosity. Furthermore, analysis of
792 the 33 off-target sites predicted by CRISPOR[60] showed that no off-target single nucleotide or structural
793 variants introduced by CRISPR-Cas9 editing. An overview of the QC performed on CRISPR-edited iPSCs
794 is provided in supplementary Fig. S7.
795
796 **Human iPSC-derived neurons and astrocytes co-culture**
797 Culture media and supplements were obtained from Stem Cell Technologies, unless mentioned

798 otherwise. Available ASE-9109 hiPSC cell line and CRISPR-edited heterozygous PLCG2 p.R953*
799 KOLF2.1J hiPSC cell line (Applied Stem Cell Inc. CA, USA) were maintained in non-treated cell culture
800 dishes/plates pre-coated with 10 µg/ml of vitronectin fresh-diluted in Cell Adhere Dilution Buffer, in
801 mTeSR+ medium fully changed daily. The ASE-9109 and KOLF2.1J NPCs were generated using the
802 embryoid body and monolayer protocols from Stem Cell Technologies, respectively. In both protocols,
803 iPSCs were induced into neural stem cells through dual SMAD inhibition, where progenitors upregulate
804 *PAX6* and *EMX1* genes, suggesting a forebrain-like phenotype[61]. NPCs were maintained in complete
805 Neural Progenitor Medium (NPM, supplemented with supplements A and B), in treated cell culture
806 dishes pre-coated with 0.001% poly-L-ornithine (PLO) diluted in water and 10 µg/mL laminin diluted in
807 0.01 M PBS with Ca^{2+} and Mg^{2+}. Full media changes were performed daily. To generate NPCs stably
808 expressing shRNAs non-targeting or targeting PLCG2 gene, NPCs derived from ASE-9109 hiPSCs were
809 transduced with lentiviral shRNAs carrying an antibiotic resistance cassette (pLV-Hygro-U6>non-
810 targeting_shRNA#1: CCTAAGGTTAAGTCGCCCTCG and pLV-Hygro U6>shPLCG2_shRNA#1:
811 CAGTTCCATCTCTTCTATAAA, Vector Builder) 4 h after seeding at Multiplicity of Infection (MOI) 4. Two
812 days after the transduction, Hygromycin (500 µg/mL, Invitrogen) was added to the cell medium and
813 kept until selection was complete.
814 Mixed cultures of human induced neurons and astrocytes were obtained from shRNA-transduced NPCs
815 after 3/4 weeks of spontaneous differentiation. For immunoblotting and immunostaining, 70,000-
816 100,000 NPCs/wells were plated in PLO/Laminin pre-coated 24-well cell imaging plates (Eppendorf,
817 0030741005) or 24-well cell culture plates (Greiner, 662160). For microfluidic devices, 30,000-40,000
818 NPCs for synaptic density analysis were seeded in both chambers of pre-coated PLL/Laminin
819 microfluidic chips. For MEA plates, a 5 µL drop of 25,000-30,000 cells was placed on the top of the
820 electrodes, and medium was added after a minimum of 30 minutes to allow the cells to attach. Cells
821 were kept in complete NPM containing 10 µM of Y-27632 ROCK Inhibitor for 24 h, before adding an
822 equal volume of complete BrainPhys medium (supplemented with N2, SM1, BDNF, GDNF, laminin,
823 dibutyryl-cAMP, and ascorbic acid)[62]. Cells were maintained in a tissue culture incubator at 37°C with
824 5% CO_2, and half-media changes were performed bi-weekly with Brainphys for 4 weeks. Our snRNA-
825 seq data confirmed that these cultures showed a predominant forebrain identity, as well as a possible
826 differentiation towards a hippocampal granule lineage (supplementary Fig. S8d).
827
828 **HCS shRNA library**
829 A HCS was performed to assess the impact of a lentiviral Mission pLKO,1-shRNA library targeting 198
830 AD-associated genes on synaptic density. The detailed methodology of our HCS was published
831 elsewhere[16]. The screening was organized in two parts: (i) 105 genes reported in 2019[63], and (ii) 93
832 genes reported in 2022[6]. These genes were selected using The Allen Brain Human MTG SmartSeq
833 Dataset (https://portal.brain-map.org/atlases-and-data/rnaseq) to limit our analysis to genes
834 expressed in brain cells. Non-coding genes, and genes with no rat homologs were also excluded. PNCs
835 were transduced at MOI 2 or 4, and the HCS was performed three times using three independent
836 neuronal cultures. A shRNA targeting Synaptophysin (shSyp, Mission, NM_009305 TRCN0000379864,
837 GGTGGTTATCAACCCGATTAC), and a non-targeting shRNA (shNT, Mission, shC002V,
838 CAACAAGATGAAGAGCACCAA) were used as positive and negative controls, respectively.
839
840 **shRNA and cDNA transduction of neuronal cultures**
841 Primary neuronal cultures (PNCs) were transduced on DIV1 with lentiviral Mission pLKO,1-shRNA
842 vectors (Merck) at MOI2 or MOI4. Viral constructs were added to pre-warmed supplemented culture

843 media with 4 µg/mL polybrene (hexadimethrine bromide, Sigma). Culture media was removed and
844 transduction mixture was added to each well to reach 20 µL final volume for 384-well plates or 250 µl
845 final volume for 24-well plates. PNCs were incubated for 6 h before equal volumes of fresh pre-
846 warmed culture media were added.
847 For Neural Progenitor Cells (NPCs) transduction with shNT and shPLCG2, viral constructs were diluted
848 in cell culture medium and directly added to NPCs. For rescue experiments, shNT NPCs and shPLCG2
849 NPCs were transduced on the first day of the differentiation with a lentiviral control vector (pLV[Exp]-
850 CAG>{empty}/Myc:T2A:EGFP, Vector Builder) or a lentiviral vector expressing a shRNA- resistant
851 PLCG2 cDNA (pLV[Exp]-CAG>{PLCG2)}/Myc:T2A:EGFP, Vector Builder).
852
853 **Immunostaining**
854 Cells were fixed with 4% paraformaldehyde (EMS, Hatfield, PA) for 20 min at RT, permeabilized with
855 0.3% Triton X-100 in PBS for 5 min at RT, and blocked with 5% normal donkey serum (Jackson
856 ImmunoResearch) and 0.1% Triton X-100 for 1 h at RT. Alternatively, neurons in 384-well plates were
857 blocked with 2.5% BSA and 0.1% Triton X-100 for 2 h at RT. Cells were washed with PBS between each
858 step. For 384-well plates, washes were automated using an automated platform (Works automation
859 control software (Agilent), Direct Drive Robot (Agilent), Plate washer (BioTek, EL406)). After blocking,
860 neurons were incubated overnight at 4°C with the following primary antibodies: Chicken or Guinea-
861 Pig anti-Homer 1 (Synaptic Systems, 160006 and 160004), Guinea-Pig or Mouse anti-Synaptophysin
862 (Synaptic Systems, 101004 and 101011), Mouse or Chicken or Guinea pig anti-MAP2 (Synaptic
863 Systems, 188011, 188006 and 188004), Rabbit anti-alpha Tubulin 4 (Abcam, ab18251), Guinea-Pig
864 anti-GFAP (Synaptic Systems, 173004). After washes with PBS, cells were incubated 2h at RT with the
865 following secondary antibodies: Donkey anti-Chicken Alexa 488 or 647 (Jackson Immunoresearch, 703-
866 545-155 and 703-605-155), Donkey anti-Rabbit Alexa 488 or 647 (Jackson Immunoresearch, 711-645-
867 152 and 711-605-152), Goat anti-Guinea- Pig Alexa 555 (Life technology, A21435), Donkey anti-
868 Guinea-Pig Alexa 405 or 594 (Jackson Immunoresearch, 706-475-148 and 706-585-148), Donkey anti-
869 Mouse Alexa 488 or 594 or 647 (Jackson Immunoresearch, 715-545-151, 711585-151 and 715-605-
870 151).
871 For immunostaining of hippocampal sections from animals injected with lentiviral vectors. At the
872 terminal timepoint mice were transcardially perfused with ice-cold saline and 4% paraformaldehyde
873 under lethal dose of ketamine-xylazine anesthesia. Then, brains were isolated and post fixed in 4%
874 paraformaldehyde and 40 µm thick coronal sections of hippocampus were prepared in vibratome (VT-
875 2000, Leica) which were then incubated overnight at 4°C with following primary antibodies: Mouse
876 anti-GFP (ab290, abcam), Mouse anti-PLCγ2 (sc-5283, Santa Cruz), Rabbit anti-iba1 (234 008, Synaptic
877 System), Mouse anti-NeuN (1B17, abcam). Further, slices were incubated with secondary antibodies
878 following 3 washes (5 min each) with PBS at RT for 2 h. If needed slices were counterstained with DAPI
879 for nuclear localization. Finally, stained sections were imaged using a Leica DM5500 TCS SPE confocal
880 microscope.
881
882 **HCS imaging and image analyses**
883 384-well plates were imaged using IN Cell Analyzer 6000 Cell Imaging System (GE Healthcare)
884 equipped with a Nikon 60× 0.95 NA objective and a CMOS camera. 16 images (2048 × 2048 pixels) per
885 well were acquired in 3 stacks (z-stack interval: 0.5 µm) from 3 channels (dsRed, FITC, and Cy5).
886 Customized image analysis software (Columbus; PerkinElmer) was used for the image analysis. MAP2
887 staining was used to define network area and Synaptophysin (Syp) and Homer1 spots were detected

within this area. A custom MATLAB (MathWorks, Natick, MA) process was used to exclude outlier fields in terms of network area or staining intensity, and to assign each Homer1 spots to the nearest Syp spot within a 1 µm cut-off distance. The density of Syp spots assigned by at least one Homer1 spot was used to calculate the synaptic density. For each well, data was normalized by the mean of non-transduced wells from the same plate. Wells with shRNA-induced toxicity, as defined by normalized network area < 0.4, were excluded from the analysis. Assay quality was assessed using β-score calculated according to $\beta = \frac{\mu_{shNT} - \mu_{shSyp}}{\sigma^2_{shNT} + \sigma^2_{shSyp}}$, where μ and σ are the mean and standard deviation of Syp density in control wells treated with shNT and shSyp, and only plates with a β-score > 1 were analyzed. After all screenings were performed, mean and standard error of the mean (SEM) of normalized synaptic density were calculated for each shRNA that did not affect network quality in at least 2 screenings. shRNAs that potentially affect synaptic density were determined as those belonging to the top or bottom 2.5% tiers.

Microfluidic chip fabrication

Masters of microfluidic devices were fabricated through photolithography as previously described[64]. Devices were cast from polydimethylsiloxane (PDMS, Sylgard 184, Dow Corning, Midland, MI) and irreversibly bonded to glass coverslips using an O_2 plasma generator (Diener, Ebhausen, Germany). Prior to cell culture, devices were sterilized under UV (Light Progress, Anghiari, Italy) for 20 min, and coated either with 0.1 mg/ml poly-D-lysine (PDL, Sigma) diluted in borate buffer for PNCs or with poly-L-lysine (PLL, Sigma) diluted in borate buffer followed by 10 µg/mL laminin (CC095, Sigma- Aldrich) diluted in 0.01 M PBS with Ca^{2+} and Mg^{2+} (Gibco, ThermoFisher Scientific) for NPCs. For quantification of synapses, tricompartment microfluidic devices that isolate the neuronal network from cell bodies were used[17]. At least two devices were employed for each experimental condition and at least three independent cultures were performed.

Synapse imaging and analysis

Synaptic compartments of microfluidic chips were imaged *via* Spinning Disk XLight V3 microscope (Nikon), using a 60× objective and a *z*-stack interval of 0.2 µm. Images were deconvoluted using Huygens Professional (Scientific Volume Imaging) and analyzed using Imaris (Bitplane, Zürich, Switzerland) by reconstructing Syp and Homer1 puncta in 3D. The relative positions of all puncta were analyzed using the custom MATLAB process described before to evaluate the synaptic density[17]. Statistically significant outliers were calculated and excluded, using the median absolute deviation method (±3 MAD). Immunostained 24-well plates were imaged *via* Spinning Disk XLight V3 microscope (Nikon), using a 40× objective and a *z*-stack interval of 0.3 µm.

Synapse fractionation

7×10^7 primary rat cortical cells were resuspended in a cold buffer containing 0.32 M sucrose and 10 mM HEPES, pH = 7.4, and were centrifuged at 1000× *g* for 10 min. The resulting supernatant was concentrated at 12,000× *g* for 20 min to remove the cytosolic fraction. Then, the resulting pellet was resuspended in a second solution (4 mM HEPES, 1 mM EDTA, pH = 7.4) and centrifuged twice at 12,000× *g* for 20 min. The new pellet was incubated in a third solution (20 mM HEPES, 100 mM NaCl, 0.5% Triton X-100, pH = 7.2) for 1 h at 4°C with mild agitation and then centrifuged at 12,000× *g* for 20 min. The supernatant collected corresponds to the triton-soluble non-PSD fraction. The remaining pellet was resuspended and incubated in a buffer containing 20 mM HEPES, 0.15 M NaCl, 1% Triton

932 X-100, 1% deoxycholic acid, 1% SDS, pH = 7.5 for 1 h at 4 °C, and then centrifuged at 10,000× *g* for 15
933 min to obtain a supernatant containing the triton-insoluble PSD fraction. The cytosolic, non-PSD, and
934 PSD fractions were then analyzed by immunoblotting.
935
936 **Immunoblotting**
937 Protein quantification was performed using the BCA protein assay (ThermoFisher Scientific). Equal
938 amounts (5–20 µg) of cell lysate were collected in RIPA buffer (0.05 M Tris, 0.15 M NaCl, 1% NP-40,
939 0.1% SDS, 1 mM sodium orthovanadate, and 0.5% sodium deoxycholate, pH = 7.4) containing protease
940 inhibitors (Complete mini, Roche Applied Science, Penzberg, Germany), lithium dodecyl sulfate
941 (ThermoFischer Scientific), and reducing agent (Invitrogen). Samples were sonicated at 60% and
942 denaturated at 95°C for 5 min. Protein extracts were separated in 4-12% Bis-Tris, or 3-8 % Tris-Acetate
943 SDS–polyacrylamide gels (NuPAGE, Thermo Scientific) and transferred on to nitrocellulose membranes
944 (Bio-Rad). Membranes were blocked in SuperBlock (ThermoFisher Scientific) for 1 h at RT and
945 incubated with primary antibodies at 4°C overnight. The following day, membranes were incubated
946 with HRP-conjugated secondary antibodies for 2 h at RT and revealed using Immobilon Classico
947 Western HRP Substrat (Millipore) and the Amersham Imager 600 (GE Life Sciences). Optical densities
948 of bands were quantified using ImageJ. The following primary antibodies were used: Chicken anti-
949 Synaptophysin (Synaptic System, 101006), Guinea-Pig anti-PSD95 (Synaptic System 124014), Chicken
950 anti-GAPDH (Millipore, AB2302), Rabbit anti-USP6NL (ThermoFisher Scientific, PA575944), Mouse
951 anti- PSMC3 (ThermoFisher Scientific, MA538612), Rabbit anti-CSNK1G1 (ThermoFisher Scientific,
952 PA5- 205268), Rabbit anti-CYB561 (Merck, SAB2100516), Rabbit anti-SNX1 (Abcam, ab134216), Rabbit
953 anti- ICA1L (ThermoFisher Scientific, 16828054), Mouse anti-OPLAH (Santa-Cruz, sc-398205), Mouse
954 anti- NCK2 (Santa-Cruz, sc-20020), Mouse anti-PLCG2 (Santa-Cruz, sc-5283), Rabbit anti-PLCG1
955 (Abcam, ab76155), Rabbit anti-APP (Sigma, A8717), Rabbit anti-hTau (Dako, A0024), Mouse anti-
956 pTauS396/404 (P. Davies, PHF1), Mouse anti-pTauT231 (P. Davies, RZ3), Mouse anti-pTauS202/T205
957 (ThermoFisher Scientific, MN1020), Rabbit anti-pTauT217 (ThermoFisher Scientific, 10536653), Mouse
958 anti-pTauT181 (ThermoFisher Scientific, MN1050), Mouse anti-GSK-3βpY216 (BD Bioscience, 612313),
959 Rabbit anti GSK-3β (Cell Signaling, 9315), Mouse anti-ERK1/2 (Cell Signaling, 4696), Rabbit anti-
960 phospho- ERK1/2 MAPK (Cell Signaling, 9101), Rabbit anti-Akt (Ozyme, C67E7), Rabbit anti-phospho-
961 Akt(Ser473) (Ozyme, CST4060), Rabbit anti-p38MAPK (Cell Signaling, 9212), Rabbit anti-phospho-
962 p38MAPK(Thr180/Tyr182) (Cell Signaling, 4511), Rabbit anti-NRXN3 (Abcam, ab192313), and Mouse
963 anti-actin (Sigma, A1979). Secondary antibodies used for the immunoblots were Goat anti-Chicken
964 HRP (ThermoFisher Scientific, A16054), Goat anti-Guinea-pig HRP (Jackson Immunoresearch, 106-035-
965 003), Goat anti-Rabbit HRP (Jackson Immunoresearch, 111-035-003) and Goat anti-Mouse HRP
966 (Jackson Immunoresearch, 115-035-003).
967
968 **Alpha-LISA measurements**
969 hNC culture media were collected at 4 weeks of differentiation to dose Aβ using Alpha-LISA assays
970 (Alpha-LISA Amyloid β1–X Kit, AL288C, PerkinElmer) according to the manufacturer's instructions. 5 µL
971 of cell medium or standard solution was added to an Optiplate-96 microplate (PerkinElmer), incubated
972 with 5 µL of 10X mixture of acceptor beads and biotinylated antibody for 1 h at RT, and then by 40 µL
973 of 1.25X donor beads for 30 min at RT. Luminescence was measured using an EnVision-Alpha Reader
974 (PerkinElmer) at 680 nm excitation and 615 nm emission wavelengths. Aβ concentrations were
975 normalized by the quantity of protein measured using BCA Protein Assay (Thermo Scientific, 23225).
976

977 **Microelectrode array recordings and analyses**

978 PNCs were cultured on PDL/Laminin pre-coated MEA 96-well plates (CytoView MEA 96, Axion
979 Biosystems, USA) and extracellular action potentials were recorded at DIV21 in three independent
980 cultures. hNCs were cultured on PLO/Laminin pre- coated MEA 24 or 48-well plates (CytoView MEA 24
981 or 48, Axion Biosystems, USA) and recorded at DIV28 in three independent cultures using the
982 MaestroPro (Axion Biosystems, Inc, USA). Signals were recorded for 5 min, and we performed multi-
983 unit analysis considering transient potentials detected using 6 standard deviations adaptative
984 threshold crossing methods, and bursts defined as a minimum of 5 spikes in 100 ms. PNCs with mean
985 firing rate <0.2 Hz, hNCs with mean firing rate < 0.1 Hz, and outliers detected with Matlab were
986 excluded from the analysis.

987

988 **Morphometric analysis of mouse DG granule cells**

989 10 male control mice (littermates of APP/PS1 mice) aged between 3-4 months old with a body weight
990 of 36.0±1.4 g, were used in this study. In order to silence the plcg2 gene in mice we have injected
991 lentiviral constructs expressing either a shRNA against PLCG2 (CAGTTCCATCTCTTCTATAAA, Vector
992 Builder) or a non-targeting (NT) shRNA (CAACAAGATGAAGAGCACCAA, Vector Builder), combined with
993 GFP expressed under the control of the PGK promoter, in the dorsal dentate gyrus through stereotaxic
994 manipulation. To compare the efficacy of transduction of both LV constructs, we injected in a same
995 mouse LV-plcg2shRNA and LV- scramble in the ipsi- and contra-lateral sides, respectively. After 27 days,
996 mice were transcardially perfused, and the brain was isolated and post-fixed in paraformaldehyde
997 (PFA, 4%). Next, 40 -µm-thick sections were prepared with vibratome, immuno-stained and imaged for
998 expression of NeuN and GFP. To analyze the morphology of GFP expressing DG granule cells, we used
999 a confocal microscope (DM5500 TCS SPE, Leica Microsystems) to acquire z-stacks at randomly chosen
1000 positions in the supra or infrapyramidal blade of DG. Images were obtained with a 63× NA 1.4 objective
1001 and regular photomultipliers. Spine density was measured in four animals with 13 fields at high
1002 magnification with >2X zoom in SP1 confocal, at least 2-3 neurites per field. In order to analyze the
1003 dendritic and spine morphometry we have used neuronstudio (ver. 0.9.92 64 bit)[65] and ImageJ[66] for
1004 reconstruction as well as analysis. Subjective investigation of GFP marker co-expressing with the shRNA
1005 construct did not show any non-neuronal cell fluorescence up on excitation with 488 nm light source.
1006 To check for transduction of microglial cells by the lentiviral construct used for *in-vivo* experiments, we
1007 have measured colocalization of IBA1 (with an anti-IBA1 antibody) and GFP immunoreactivity in the
1008 contralateral shNT and shPLCG2 injected mice brain.

1009

1010 ***In vivo* viral gene transfer in the DG**

1011 Mice (P22–P30) were anesthetized by isoflurane inhalation and injected with buprenorphine to
1012 prevent post-surgery pain. 1 µL of either LV-shNT or LV-shPLCG2 solution (5×10^6 lentiviral particles)
1013 was injected using a micropump and syringe (Nanofil WPI) at the rate of 100 nL/min in the DG (Y: 2.2
1014 mm from lambda; X: ± 2.0 mm from sagittal suture; Z: 2.0 mm from the skull) to infect GCs in the dorsal
1015 hippocampus. In the acquired images, we have calculated dual positive cells, i.e., IBA1 expressing
1016 transfected (GFP+) cells in three animals separately, with contralateral intrahippocampal injection of
1017 LV-shNT or LV-shPLCG2 viral constructs using stereotaxic manipulation. For cell counting we have used
1018 four random microscopic fields in high magnification. Signals were counted in FIJI using 'multipoint
1019 tool' in z-projection from image stacks.

1020

1021 **Electrophysiology analysis of mouse DG slices**

1022 For electrophysiological recordings, slices were prepared at least 3 weeks post-injection. Mice were
1023 anesthetized using ketamine/xylasine mix (100 mg/kg / 10 mg/kg; i.p.) and perfused transcardially with
1024 ice cold artificial cerebrospinal fluid (aCSF) for 40–60 s. The brain was quickly removed and placed in
1025 ice-cold aCSF containing the following (in mM): 120 NaCl, 26 $NaHCO_3$, 2.5 KCl, 1.25 NaH_2PO_4, 2 $CaCl_2$,
1026 1 $MgCl_2$, 16.5 glucose, 2.8 pyruvic acid, 0.5 ascorbic acid, pH 7.4 adjusted by saturating with carbogen
1027 (95% O_2 and 5% CO_2), and an osmolarity of 305 mOsm. The slices were then transferred to a recording
1028 chamber where they were submerged and perfused with an extracellular recording solution containing
1029 the following (in mM): 125 NaCl, 2.5 KCl, 1.35 NaH_2PO_4, 2 $CaCl_2$, 1 $MgCl_2$, 16 glucose, 26 $NaHCO_3$
1030 continuously oxygenated (95% O_2 and 5% CO_2). The recordings were made at RT. Whole-cell patch-
1031 clamp recordings (3–4 MΩ electrodes, − 70 mV holding potential) were made from GFP expressing DG
1032 granule cells visualized by infrared video-microscopy and epifluorescence. Patch clamp electrodes
1033 were pulled out from borosilicate glass (GF 150 F-10). For voltage-clamp recordings, the internal
1034 solution contained the following (in mM): 140 $CsCH_3SO_3$, 2 $MgCl_2$, 4 NaCl, 5 phospho-creatine, 2
1035 Na_2ATP, 0.2 EGTA, 10 HEPES, and 0.33 GTP adjusted with CsOH (300 mOsm, pH 7.3). For current-clamp
1036 recordings, a K+-based internal solution containing (in mM) was used: 115 K-gluconate, 10 KCl, 0.2
1037 EGTA, 10 HEPES, 15 phospho-creatine, 4 MgATP and 0.3 NaGTP adjusted with KOH (300– 305 mOsm,
1038 pH 7.3). The access resistance was <20%. TTX (500 nM) was added to the bath for miniature EPSCs
1039 recording. MOhms and the experiment was discarded if it changed by >20%. Recordings were made
1040 using an EPC10.0 amplifier (HEKA Elektronik), filtered at 0.5–1 kHz and analysed using IGOR Pro and
1041 Neuromatic V2.6 softwares. Evoked AMPA-EPSCs and NMDA-EPSCs were recorded following electrical
1042 stimulation of the perforant path (at 0.1 Hz), with an electrode positioned in the molecular layer of the
1043 DG, at a membrane potential of -70 mV and +40 mV (in the presence of 10 µM NBQX), respectively. All
1044 animal experiments were approved by the local ethical committee of the Institut Pasteur de Lille and
1045 according to regulations of the University of Bordeaux/Centre National de la Recherche Scientifique
1046 (CNRS) Animal Care and Use Committee.

1047

1048 **Whole exome sequencing data**

1049 Written informed consent was obtained from study participants or, for those with substantial cognitive
1050 impairment, from a caregiver, legal guardian, or other proxy, and the study protocols for all
1051 populations were reviewed and approved by the appropriate local Institutional Review Boards[67]. The
1052 ADGEN cohort has been collected for a study focusing on the identification of novel Alzheimer's
1053 disease-associated genes and pathways using existing clinical cohorts from Eastern Finland. Research
1054 Ethics Committee of Northern Savo, Finland has approved ADGEN study; approval statement
1055 420/13.02.00/2016.

1056 ADGEN cohort comprised 527 AD patients (mean age at onset of AD 72.4 ± 7.9 years, range 43 to 91;
1057 65% women) from Eastern Finland. These AD patients were examined at the Department of Neurology,
1058 Kuopio University Hospital and they all fulfilled the NINCDS-ADRDA criteria for probable AD[67]. Whole-
1059 exome sequencing (WES) data were generated from ADGEN cohort at the Broad Institute, the Baylor
1060 College of Medicine's Human Genome Sequencing Center, and Washington University's McDonnell
1061 Genome Institute[68]. Multiallelic sites were converted into biallelic variants and then left-aligned using
1062 bcftools 1.10. Variants with variant quality score log-odds (VQSLOD) less than -2 or inbreeding
1063 coefficient less than -0.3 were excluded. All variants included in final analysis had genotype read depth
1064 of at least 10 and genotype quality at least 25[69]. Ensembl Variant Effect Predictor (version v98)

(https://www.ensembl.org/info/docs/tools/vep/index.html) was used to predict pathogenicity of PLCG2 variants. To confirm the two nonsense variants in PLCG2 gene identified with WES, DNA was extracted from the blood samples of the carriers using QIAamp DNA Blood Mini Kit (51104, Qiagen). To confirm SNP rs368241065 (C>T, p.R953*), PCR was conducted around the target site by using the following primers: 5'-CACCCACATTGCAACCCTAC-3', 5'- CTTCGGTCCTCTCATCCCTC-3'. After purification with NucleoSpin® Gel and PCR Clean-up kit (#740609.50, Macherey-Nagel), the PCR product was sequenced at Macrogen Europe (Amsterdam, the Netherlands) with primer 5'-AGAGGGCAAGAGTCCACAG-3'. Novel variant (C>T, p.Q816*) was directed to whole genome sequencing at Novogene Europe. We used the 'European (Finnish)' non-neuro subset of the gnomAD v2.1.1 exome dataset as a control cohort (n= 8,707). This cohort contains only samples, which were not collected as part of a neurologic or psychiatric case/control study, or samples that were collected as part of a neurologic or psychiatric case/control study but designated as controls. We identified therein three participants who carried any predicted PLCG2 LoF SNV or indel variants.

WES data from Alzheimer Disease European Sequencing (ADES) consortium cohort comprising of 8,732 AD patients and 8,955 control individuals were analyzed by focusing on PLCG2 LoF variants and the same pipeline and QC step were applied as described in[7]. A total of five different PLCG2 LoFs were found in France, The Netherlands and the UK. There were nine carriers of any of the five *PLCG2* LoF variants among 8,732 cases and one carrier among 8,955 controls. All the LoF variants are fully described in supplementary Table S2.

Meta-analysis of the PLCG2 LoF variants in ADGEN and ADES cohorts was performed using the metabin function of the R-package meta (v7.0.0)[70] using the 'Mantel-Haenszel' method and 'OR' as the summary measure.

RNA sequencing in blood

RNA was extracted from the frozen blood of AD patient (age of onset = 60 years) carrying *PLCG2* p.Q816* variant and from four probable AD patients[67] without PLCG2 LoF variants (mean age of onset = 61±1.4 years; range 60-63) using NucleoSpin® RNA Blood kit (#740200.10, Macherey-Nagel) according to the kit instructions. Library preparation and RNA sequencing was conducted at Novogene Europe (Cambridge, UK) with an Illumina high-throughput sequencing platform. The 150 nt pair-end RNA-seq reads from the 21.7–28.9 million sequenced fragments per sample were quality controlled using FastQC (version 0.11.7) https://www.bioinformatics.babraham.ac.uk/projects/fastqc/). Reads were trimmed with Trimmomatic (version 0.39)[71] to remove Illumina sequencing adapters and poor quality read ends, using the following essential settings: ILLUMINACLIP:2:30:10:2:true, SLIDINGWINDOW:4:10, LEADING:3, TRAILING:3, MINLEN:50. The trimmed reads were aligned to the Gencode human transcriptome version 38 (for genome version hg38) using STAR (version 2.7.9a)[72] with essential non-default settings: -seedSearchStartLmax 12, -alignSJoverhangMin 15, -outFilterMultimapNmax 100, -outFilterMismatchNmax 33, -outFilterMatchNminOverLread 0, -outFilterScoreMinOverLread 0.3, and -outFilterType BySJout. The unstranded, uniquely mapping, gene-wise counts for primary alignments were collected in R (version 4.3.2) using Rsubread::featureCounts (version 2.16.1)[73], totaling 14.2 to 18.0 million per sample. Read counts for PLCG2 gene were normalized for differences in sequencing depth using size factors calculated by estimateSizeFactors (from DESeq2 version 1.38.3)[74].

AD hallmarks in human brain and CSF samples

Human post-mortem brain samples were originally obtained from Kuopio University Hospital and investigated within Memory polyclinic research projects. Following autopsy, brains were fixed in buffered 10 % formalin for at least one week. Tissue blocks were prepared, embedded in paraffin, and used for evaluation of AD-related pathology and classified according to Braak staging as described before[75]. Detailed information of the cohort and handling of the samples have been provided in several previous publications[76–78]. Individual carrying the p.R953* variant in *PLCG2* was analyzed together with five matched controls. All analyzed subjects were females (mean age 84.3±4.03), APOE ε3/4, diagnosed with clinical dementia, and defined as Braak stage VI in the neuropathological examination.

Immunohistochemistry. Paraffin embedded inferior temporal lobe samples were serially sectioned in 7 µm thickness. The sections were deparaffinized in xylene and rehydrated in graded alcohol series. For IBA1/Aβ co-staining, sections were processed and stained with rabbit anti-IBA1 (1:1000, #019–19,741, FUJIFILM Wako Chemicals Europe GmbH) and mouse anti-Aβ (1:500, anti-β-amyloid 17–24, clone 4G8, #800712, 1:500, Biolegend) following the procedure explained elsewhere[79].
For fluorescent staining, antigen retrieval was performed in 10 mM Tris – 1 mM EDTA buffer, pH 9.0 in pressure cooker for 10 min for all sections except those used for p-Tau staining. Additional antigen retrieval step in 80 % formic acid (20 min, RT) was carried out for sections used for CD68/Aβ/IBA1 staining. Autofluorescence was quenched using TrueBlack lipofuscin autofluorescence quencher (#23007, Biotium). Target proteins were visualized by following primary antibodies: goat anti-Apolipoprotein E (1:1000, #178479, Merck Millipore), goat-anti IBA1 (1:1000, #ab5076, Abcam), mouse anti-Aβ (1:500, anti-β-amyloid 17–24, clone 4G8, #800712, Biolegend), rabbit anti-GFAP (1:1000, #Z0334, Dako), rabbit anti-P2RY12 (1:1000, #HPA014518, Sigma Aldrich), and mouse anti-phospho-tau detecting phosphorylated Ser202, Thr205, and Ser208 residues (1:1000, B6, produced in house[79–81]) coupled with appropriate species-specific secondary antibodies: donkey anti-goat IgG Alexa Fluor 568 (1:500, #A-11057, Invitrogen), donkey anti-goat IgG Alexa Fluor 633 (1:500, #A21082, Invitrogen), goat anti-mouse IgG Alexa Fluor 488 (1:2000, #A-11001, Invitrogen), donkey anti-mouse IgG Alexa Fluor 568 (1:500, #A10037, Invitrogen), goat anti-rabbit IgG Alexa Fluor 680 (1:500, #A- 21109, Invitrogen). CD68 was visualized by rabbit anti-CD68 (1:5000, #ab213363, Abcam) followed by horse anti-rabbit biotinylated IgG (1:200, BA-1100, Vector Laboratories) and Alexa Fluor 488 Tyramide SuperBoost streptavidin kit (B40932, Invitrogen). To visualize β-sheet structures within Aβ plaques, sections were incubated 10 min in 100 µM X-34 (1,4-Bis(3-carboxy-4-hydroxyphenylethenyl)benzene, Sigma-Aldrich) in 40% ethanol, and differentiated in 80% ethanol with 0.2g% NaOH for 2 min. Nuclei were visualized with DAPI (1 µg/ml) and the sections were embedded with Vectashield Hardset or Vectashield Vibrance antifade mounting medium (H-1400 and H-1700, Vector Laboratories).

Imaging and analysis of human brain tissue. IBA1/Aβ co-stained sections were imaged with Hamamatsu NanoZoomer-XR Digital slide scanner with 20× (NA 0.75) objective (Hamamatsu Photonics K.K.). NDP.view2 software (Hamamatsu Photonics K.K.) was used for counting the number and the size of β-amyloid plaques and the number of β-amyloid plaque-associated microglia. For analysis, seven 250 µm2 blocs were randomly chosen from the grey matter area in each brain section. All plaques within the blocks were included in the analysis. Size of the β-amyloid plaques was obtained by manually outlining the plaques. Plaque-associated microglia (within or touching the plaque) were manually counted. Only microglia with clearly visible soma were included in the count. Counting and analysis was performed by investigators blinded to sample identity.

1153 P2RY12, GFAP, and B6 immunofluorescence stainings were imaged with THUNDER Imager 3D Tissue
1154 imaging system equipped with 20× objective and using the built-in computational clearing method to
1155 remove out-of-focus signal (Leica Microsystems). Seven to ten randomly selected fields of view in
1156 cortical grey matter were imaged in each sample. Images were further processed with Fiji[66] by applying
1157 background subtraction (Sliding paraboloid, Rolling ball radius 50 pixels) and Gaussian blur filtering
1158 before masking the images using the automatic threshold (Li algorithm for GFAP, Triangle for P2RY12,
1159 Moments for B6, and Li for DAPI) and measuring the immunopositive area. APOE, X-34, CD68, IBA1,
1160 and 4G8 immunofluorescence stainings were imaged with Axio Observer inverted microscope
1161 equipped with a LSM800 confocal module with Plan-Apochromat 20× or 40× (NA 0.8) objective (Carl
1162 Zeiss Microimaging GmbH). A z-stack was captured from six to eight randomly selected fields of view.
1163 A sum projection of the stack was created in Fiji, after which the background was subtracted (Sliding
1164 paraboloid, Rolling ball radius 50 pixels) and Gaussian blur filtering applied. The images were then
1165 masked using the automatic threshold algorithm (Triangle for APOE, IBA1, and 4G8, Moments for X-34
1166 and CD68), and immunopositive area was measured. All imaging and analyses were performed by
1167 investigators blinded to sample identity.
1168
1169 *Processing and analysis of frozen brain tissue samples.* Frozen brain tissue from the same individuals
1170 were homogenized, and proteins were extracted as described previously[76]. The protein concentration
1171 of the lysates was measured with the Pierce BCA Protein Assay Kit (#23227, Thermo Fisher Scientific).
1172 18 µg of total protein per sample were denatured at 55°C for 10 min with NuPAGE LDS Sample Buffer
1173 (#NP0007, Invitrogen). Proteins were separated on NuPAGE 4–12% BisTris Midi Protein Gels
1174 (#WG1202BOX, Invitrogen) and transferred onto PVDF membranes (#IB24001, Thermo Fisher
1175 Scientific) with an iBlot 2 device (IB21001, Thermo Fisher Scientific). Blot was probed overnight at +4°C
1176 with PLCγ2 (1:200, clone B-10, #sc-5283, Santa Cruz) and β-actin (1:1000, #ab8226, Abcam) antibodies.
1177 After incubation with mouse IgG horseradish peroxidase linked secondary antibody (1:5000,
1178 #GENA931, Merck) for 1 h, proteins were detected with ECL Select Western Blotting Detection Reagent
1179 (#12644055, Merck) and a ChemiDoc Imaging System (Bio-Rad Laboratories). Image Lab Software 6.0.1
1180 (Bio-Rad Laboratories) was used to quantify protein levels. The levels of PLCγ2 were normalized to that
1181 of β-actin within each sample. $A\beta_{42}$ levels were measured from soluble fraction using HRP-conjugated
1182 antibody-based Human/Rat β-Amyloid 42 (High Sensitive, #29062601, Wako) ELISA Kit as has been
1183 described before[78]. $A\beta_{42}$ concentrations were normalized to total protein concentration of the same
1184 sample.
1185
1186 *CSF analyses.* $A\beta_{42}$, total-tau (tau), and phosphorylated-tau (p-tau) levels in the CSF were measured
1187 using Innotest β-amyloid 1-42, Innotest hTau Ag, and Innotest Phospho-tau 181P ELISA kits
1188 (Innogenetics, Ghent, Belgium) according to the protocol described previously[77,78].
1189
1190 **Analysis of single-nucleus RNA-sequencing datasets of human brains**
1191 We obtained two publicly available datasets of single-nucleus RNA-seq on human brain tissue,
1192 published by Li et al. 2025[22] (GSE237718 from GEO) and Leng et al. 2021[23] (syn21788402 from
1193 Synapse). The former was performed on temporal cortex tissue, and the latter was performed on
1194 entorhinal cortex and superior frontal gyrus. Analysis was performed using the R package Seurat[82]. For
1195 Li et al. 2025[22], each individual's data was read, keeping cells with at least 200 detected features and
1196 fraction of mitochondrial genes less than 10%, and keeping features detected in at least 10 cells. Data

1197 were SCTransformed while regressing on percent mitochondrial genes[83]. FindNeighbors was run using
1198 30 principal component analysis (PCA) dimensions, and FindClusters with resolution 0.35. Clusters
1199 were classified into the following cell types using a set of rules based on marker genes: microglia
1200 (PTPRC), astrocytes (SLC1A2), oligodendrocytes (PLP1), oligodendrocyte precursor cells (VCAN),
1201 inhibitory neurons (GAD1 minus VCAN-positive clusters), excitatory neurons (CAMK2A minus GAD1-
1202 positive clusters), and vascular/endothelial cells (CLDN5). For Leng et al. 2021[23], cells were already
1203 annotated with cell types.
1204
1205 **Single-nucleus RNA-sequencing of hNCs cultures**
1206 *Nuclei isolation.* The isolation of hNCs nuclei was conducted on ice using pre-cold buffers, followed by
1207 centrifugation at 500 rcf and 4°C for 15 min. First, cells were resuspended in lysis buffer: 10 mM Tris-
1208 HCl, 10 mM NaCl, 3 mM $MgCl_2$, 0.1% NP40 and 0.04 U/µl RNase OUT (Invitrogen, 10777019). The nuclei
1209 pellet was subsequently washed three times with nuclei wash buffer (1× DPBS, 1% BSA, and 0.04 U/µl
1210 RNase OUT). The cells were then filtered through a 40 µm Flowmi strainer (Merck, BAH136800040-
1211 50EA) and fixed using the Single Cell Fixed RNA Sample Preparation Kit (10X genomics, PN-1000414).
1212 The nuclei were preserved in 10X nuclei preservation buffer and stored at -80°C until four independent
1213 differentiations were completed.
1214
1215 *Library preparation and sequencing.* The day of the hybridization protocol, samples from all four
1216 conditions were thawed and processed in parallel. Each experimental condition (shNT, shPLCG2, WT
1217 and R953*) was hybridized using one of the four probes from the Chromium Next GEM Single Cell Fixed
1218 RNA Human Transcriptome Probe Kit (PN-1000420; 10X Genomics). Samples were then pooled to
1219 create a single mix containing all four conditions and to target 40,000 encapsulated nuclei per lane
1220 (n=4 lanes) according to the manufacturer's protocol. Pooled nuclei were then encapsulated by using
1221 Single Cell TL v1 Gel Bead (PN-2000538; 10X Genomics) and Next GEM Chip Q (PN-2000518; 10X
1222 Genomics) on the Chromium iX. SnRNA-seq libraries were prepared by using the PTC-200 Thermal
1223 Cycler (MJ Research) and by following the Fixed RNA Profiling Reagent Kit's user guide (CG000527 Rev
1224 F; 10X Genomics). Library quality was assessed with the Bioanalyzer 2100 (Agilent) and their cDNA
1225 quantity was assayed using the Quant-IT™ 1X dsDNA HS Assay Kit (Ref Q33232; Invitrogen). All four
1226 libraries were combined in equimolar quantities for a single sequencing pool. This pool was sequenced
1227 (BGI, Hong Kong) according to the manufacturer's instructions (28:10:10:90, R1:i7:i5:R2) targeting a
1228 depth of ~60k reads/nuclei.
1229
1230 *snRNA-seq data preprocessing and annotation.* Sequencing reads for the four multiplexed libraries
1231 have been processed using Cellranger Multi (10X Genomics) in Multiplex Flex mode using associated
1232 human genome reference refdata-gex-GRCh38-2024-A and Human Transcriptome probes set
1233 v1.1.0_GRCh38-2024-A, calling in average 15k cells per sample, median of 2500 genes and 4000 UMis
1234 detected per cell. We then used Seurat (V5.2.1)[82] to process the generated gene expression matrices.
1235 To remove low quality and aggregated nuclei, we removed all nuclei with more than 8% mitochondrial
1236 count or number of total count exceeding 100k. In addition, we removed nuclei with both low gene
1237 detection (less than 1500) and having high mitochondrial RNA percentage (greater than 2%), likely
1238 reflecting high mitochondrial contamination over degraded nuclei (supplementary Fig S8a,b). We
1239 observed at this stage that one replicate of shPLCG2 (shPLCG2_4) had a strong mitochondrial
1240 percentage (median = 3% while all other samples had <1%) and low RNA and gene counts; we thus
1241 excluded this replicate as well as the associated control (shNT_4) from the analysis. Then, the gene

expression matrices were normalized using Seurat::SCTransform() with default parameters but regressing out for mitochondrial percentage. PCA was performed on the residuals of the 3000 most variable genes, and harmony::RunHarmony() (1.2.0)[84] was used to reduce influence of batch effect on PCs by correcting for sample specific variability. The 20 first harmony corrected component was used to generate a Shared Nearest Neighbor graph using Seurat::FindNeighbors() and cluster nuclei on this graph with Louvain algorithm using Seurat::FindClusters() with resolution of 0.5. UMAP with Seurat::RunUMAP() was then performed to generate a two-dimension space non linearly representing the gene expression variability between nuclei. A total of 23 clusters were identified (supplementary Fig S8c) with mix of samples within each cluster (supplementary Fig. S8d, g). These clusters were annotated based on canonical neuronal markers expression in each cluster (supplementary Fig. S8f). From these 23 clusters, we identified: Astrocytes, subdivided into 4 subpopulations (steady state: clusters 1, 6, 7 and 18; proliferative: clusters 4 and 8; immature: cluster 10; with VLMC potential: clusters 13 and 22); Excitatory Neurons (clusters 12, 19 and 20); Inhibitory Neurons (clusters 5, 14 and 17); NPCs (cluster 9); Vascular leptomeningeal cells (VLMC, cluster 11); and Fibroblasts (cluster 21). Cluster 0 contained a mix of excitatory and inhibitory neurons and was therefore subdivided into two clusters based on the expression of glutamate transporter SLC17A6 and the GABAergic enzymes GAD1/2. Cluster 16, expressing markers of more than one cell type and with greater RNA content than others, was deemed as doublet cells and removed. Clusters 2, 3 and 15 having low RNA content, high mitochondrial RNA percentage, low cell type identity and/or expressing stress markers (Chaperone/ heat shock protein gene family, stress granules TIA1) were filtered out as well (supplementary Fig. S8e). The resulting filtered matrix and clusters alongside with the raw feature barcode matrices were used to estimate ambient RNA contamination in each sample using SoupX (1.6.2)[85]. Probes based snRNA-seq assay having higher gene detection but also higher ambient RNA level compared to standard polyA based mRNA capture technic, we increased stringency in determining contamination threshold using for each sample SoupX::autoEstCont() with tfidfMin=.95 , soupQuantile =0.6, priorRho = 0.1, and contaminationRange = c(0.05,0.8) parameter to automatically estimate ambient RNA level. The estimated ambient level was 14% on average (min: 5.1%, max: 34%) across samples. We then used SoupX::adjustCounts() to correct the gene expression matrix accordingly, and we further ensured no impact on downstream differential analysis using the ambient RNA level as covariate.

Neuronal maturation score calculation. We calculated a neuronal maturation score using a published neuron-specific maturation gene set (MS-NS, 25 genes)[86] and performed cell level enrichment analysis using UCell[87], AddModuleScore_UCell function with parameter maxRank=1500. We then computed the average score per donor and cell type.

Differential expression and pathway enrichment analysis. Cell type-specific differential expression analyses comparing R953* *vs* WT and shPLCG2 *vs* shNT were performed using DESeq2(v1.40.2)[74] and the SoupX corrected-count matrix. For each cell type, the genes were filtered to keep only those for which more than 100 nuclei or 10% of the nuclei have at least 5 counts. The counts were then aggregated per sample, and the resulting pseudobulk count matrix was further filtered out by keeping only genes with more than 50 CPM in at least 20% of the samples. Negative binomial model-based regression using DESeq2 was then performed to estimate effect of the treatment or genotype, correcting for average mitochondrial RNA percentage, ambient RNA contamination rate, and library batch. Before running DESeq2::DESeq() model fitting, the size factors (from DESeq2::estimateSizeFactors()) were estimated using the unfiltered pseudobulk matrix. Were

1287 considered as DEGs, genes with FDR <0.05 and |log2FC|>0.5. Functional enrichment analysis was
1288 performed on these DEGs using hypergeometric test (base::phyper()) and MSigDB Gene Ontology and
1289 Canonical Pathways (c2.cp.v2023 and C5.go.v2023).
1290
1291 *Regulon analysis.* We performed the TF regulon identification using pyscenic 0.12.1.[88](with grnboost2)
1292 on 20,000 randomly sampled nuclei transcriptome previously normalized and log-transformed using
1293 sc.pp.normalize total and sc.pp.log1p.[89] We used 'hg38_10kbp_up_10kbp_down_full_tx_v10' genes-
1294 motifs ranking and 'motifs-v10nr' TF motifs from cis target database
1295 https://resources.aertslab.org/cistarget/databases/homo_sapiens/hg38/refseq_r80/mc_v10_clust/g
1296 ene_based/. We then computed the cell level activity score of the identified TF regulons on the full
1297 dataset using pyscenic.aucell. The resulting score for each regulon was then averaged per sample and
1298 cell type, and Wilcoxon ranks sum test was performed to compare the conditions on selected regulons.
1299
1300 *Cell-Cell Communication.* Cell-Cell communication with ligand receptor (L/R) interaction inference was
1301 performed using CellChat (2.2.0)[34]. For each condition, replicates were first grouped into one CellChat
1302 object and communication probabilities between cell types were determined using CellChatDB.human
1303 reference excluding non-protein signaling. CellChat::identifyOverExpressedGenes,
1304 CellChat::identifyOverExpressedInteractions and CellChat::computeCommunProb were used with
1305 default parameters to measure probability of communication (interaction strength and statistical
1306 significance) based on ligand, receptor and cofactors overexpression. To filter L/R not conserved across
1307 biological replicates, CellChat::filterCommunication was used with min.samples = 3 and min.cells = 10.
1308 These measurements were aggregated at signaling pathways level using
1309 CellChat::computeCommunProbPathway. Overall incoming and outgoing signaling L/R and signaling
1310 pathway interaction strength for each cell type were then computed using
1311 CellChat::netAnalysis_computeCentrality. Difference of strength between treated and respective
1312 control condition was determined to obtain the differential incoming/outgoing interaction, where
1313 difference of strength > 0.25 was considered significant. To further confirm robustness of the
1314 differences observed across condition for the significant signaling pathways and L/R interaction, cell-
1315 cell communication inference was performed again for each sample separately, and the interaction
1316 strength per cell type was collected for each sample and compared between conditions using Wilcoxon
1317 rank sum test.

1318 *Comparison with dementia DEGs.* SEA-AD DLPFC and MTG snRNA-seq datasets were downloaded from
1319 https://registry.opendata.aws/allen-sea-ad-atlas/. Donors annotated as 'Reference' (lacking cognitive
1320 status), and with non-Caucasian ethnicity have been excluded from analysis, as well as donors with
1321 abnormal cell type distribution. Abnormal cell type distribution was measured by calculating the cell
1322 type proportion deviation from the interquartile range (IQR) and by computing the PCA of these
1323 deviation matrices. Donors with first principal component coordinates at 3 times away from the IQR
1324 were excluded from analysis. A total of 12 donors were excluded for both DLPFC and MTG regions. For
1325 each cell type, donors with more than 50 nuclei were considered. A donor level count matrix was then
1326 generated by aggregating nuclei count by donor (total number of donors kept for analysis = 70). The
1327 differential expression was performed on comparing the individuals with dementia compared to
1328 individuals without dementia using DESeq2, adjusting for sex, post mortem interval (PMI),
1329 atherosclerosis stage, library input (ng), number of PCR cycles, number of cells, median number of
1330 molecules detected per cell, average mitochondrial RNA percentage.

1331 **REFERENCES**

1332 51. Kaech, S. & Banker, G. Culturing hippocampal neurons. *Nat. Protoc.* **1**, 2406–2415 (2006).
1333 52. Pantazis, C. B. *et al.* A reference human induced pluripotent stem cell line for large-scale
1334 collaborative studies. *Cell Stem Cell* **29**, 1685-1702. (2022).
1335 53. Duncan, G. T., Balamurugan, K., Budowle, B., Smerick, J. & Tracey, M. L. Microvariation at the
1336 human D1S80 locus. *Int. J. Legal Med.* **110**, 150–154 (1997).
1337 54. Weisheit, I. *et al.* Simple and reliable detection of CRISPR-induced on-target effects by qgPCR
1338 and SNP genotyping. *Nat. Protoc.* **16**, 1714–1739 (2021).
1339 55. Garcia, M. *et al.* Sarek: A portable workflow for whole-genome sequencing analysis of germline
1340 and somatic variants. *F1000Research* **9**, 63 (2020).
1341 56. Rausch, T. *et al.* DELLY: structural variant discovery by integrated paired-end and split-read
1342 analysis. *Bioinformatics* **28**, i333-i339 (2012).
1343 57. Chen, X. *et al.* Manta: rapid detection of structural variants and indels for germline and cancer
1344 sequencing applications. *Bioinformatics* **32**, 1220–1222 (2016).
1345 58. Pedersen, B. S. & Quinlan, A. R. Duphold: scalable, depth-based annotation and curation of
1346 high-confidence structural variant calls. *Gigascience* **8**, giz040 (2019).
1347 59. Jeffares, D. C. *et al.* Transient structural variations have strong effects on quantitative traits and
1348 reproductive isolation in fission yeast. *Nat. Commun.* **8**, 14061 (2017).
1349 60. Concordet, J. P. & Haeussler, M. CRISPOR: Intuitive guide selection for CRISPR/Cas9 genome
1350 editing experiments and screens. *Nucleic Acids Res.* **46**, W242–W245 (2018).
1351 61. Chambers, S. M. *et al.* Highly efficient neural conversion of human ES and iPS cells by dual
1352 inhibition of SMAD signaling. *Nat. Biotechnol.* **27**, 275–280 (2009).
1353 62. Bardy, C. *et al.* Neuronal medium that supports basic synaptic functions and activity of human
1354 neurons in vitro. *Proc. Natl. Acad. Sci. U. S. A.* **112**, E2725–E2734 (2015).
1355 63. Kunkle, B. W. *et al.* Genetic meta-analysis of diagnosed Alzheimer's disease identifies new risk
1356 loci and implicates Aβ, tau, immunity and lipid processing. *Nat. Genet.* **51**, 414–430 (2019).
1357 64. Blasiak, A., Lee, G. U. & Kilinc, D. Neuron Subpopulations with Different Elongation Rates and
1358 DCC Dynamics Exhibit Distinct Responses to Isolated Netrin-1 Treatment. *ACS Chem. Neurosci.*
1359 **6**, 1578–1590 (2015).
1360 65. Rodriguez, A., Ehlenberger, D. B., Hof, P. R. & Wearne, S. L. Rayburst sampling, an algorithm for
1361 automated three-dimensional shape analysis from laser scanning microscopy images. *Nat.*
1362 *Protoc.* **1**, 2152–61 (2006).
1363 66. Schindelin, J. *et al.* Fiji: an open-source platform for biological-image analysis. *Nat. Methods* **9**,
1364 676–82 (2012).
1365 67. McKhann, G. *et al.* Clinical diagnosis of Alzheimer's disease: report of the NINCDS-ADRDA Work
1366 Group under the auspices of Department of Health and Human Services Task Force on
1367 Alzheimer's Disease. *Neurology* **34**, 939–944 (1984).
1368 68. Bis, J. C. *et al.* Whole exome sequencing study identifies novel rare and common Alzheimer's-
1369 Associated variants involved in immune response and transcriptional regulation. *Mol.*
1370 *Psychiatry* **25**, 1859–1875 (2020).
1371 69. Korpioja, A. *et al.* Novel Rare SORL1 Variants in Early-Onset Dementia. *J. Alzheimers. Dis.* **82**,
1372 761–770 (2021).
1373 70. Balduzzi, S., Rücker, G. & Schwarzer, G. How to perform a meta-analysis with R: a practical
1374 tutorial. *Evid. Based. Ment. Health* **22**, 153–160 (2019).
1375 71. Bolger, A. M., Lohse, M. & Usadel, B. Trimmomatic: a flexible trimmer for Illumina sequence
1376 data. *Bioinformatics* **30**, 2114–2120 (2014).
1377 72. Dobin, A. *et al.* STAR: ultrafast universal RNA-seq aligner. *Bioinformatics* **29**, 15–21 (2013).
1378 73. Liao, Y., Smyth, G. K. & Shi, W. The R package Rsubread is easier, faster, cheaper and better for
1379 alignment and quantification of RNA sequencing reads. *Nucleic Acids Res.* **47**, e47 (2019).
1380 74. Love, M. I., Huber, W. & Anders, S. Moderated estimation of fold change and dispersion for
1381 RNA-seq data with DESeq2. *Genome Biol.* **15**, 550 (2014).
1382 75. Braak, H., Alafuzoff, I., Arzberger, T., Kretzschmar, H. & Tredici, K. Staging of Alzheimer disease-

1383 associated neurofibrillary pathology using paraffin sections and immunocytochemistry. *Acta*
1384 *Neuropathol.* **112**, 389–404 (2006).
1385 76. Marttinen, M. *et al.* A multiomic approach to characterize the temporal sequence in Alzheimer's
1386 disease-related pathology. *Neurobiol. Dis.* **124**, 454–468 (2019).
1387 77. Martiskainen, H. *et al.* Effects of Alzheimer's disease-associated risk loci on cerebrospinal fluid
1388 biomarkers and disease progression: a polygenic risk score approach. *J. Alzheimers. Dis.* **43**,
1389 565–573 (2015).
1390 78. Natunen, T. *et al.* Effects of NR1H3 genetic variation on the expression of liver X receptor α and
1391 the progression of Alzheimer's disease. *PLoS One* **8**, e80700 (2013).
1392 79. Natunen, T. *et al.* Diabetic phenotype in mouse and humans reduces the number of microglia
1393 around β-amyloid plaques. *Mol. Neurodegener.* **15**, 66 (2020).
1394 80. Kemppainen, S. *et al.* Organotypic Hippocampal Slice Cultures from Adult Tauopathy Mice and
1395 Theragnostic Evaluation of Nanomaterial Phospho-TAU Antibody-Conjugates. *Cells* **12**, 1422
1396 (2023).
1397 81. Gabbouj, S. *et al.* Intranasal insulin activates Akt2 signaling pathway in the hippocampus of wild-
1398 type but not in APP/PS1 Alzheimer model mice. *Neurobiol. Aging* **75**, 98–108 (2019).
1399 82. Hao, Y. *et al.* Dictionary learning for integrative, multimodal and scalable single-cell analysis.
1400 *Nat. Biotechnol.* **42**, 293–304 (2024).
1401 83. Choudhary, S. & Satija, R. Comparison and evaluation of statistical error models for scRNA-seq.
1402 *Genome Biol.* **23**, (2022).
1403 84. Korsunsky, I. *et al.* Fast, sensitive and accurate integration of single-cell data with Harmony.
1404 *Nat. Methods* **16**, 1289–1296 (2019).
1405 85. Young, M. D. & Behjati, S. SoupX removes ambient RNA contamination from droplet-based
1406 single-cell RNA sequencing data. *Gigascience* **9**, giaa151 (2020).
1407 86. Shan, X. *et al.* Fully defined NGN2 neuron protocol reveals diverse signatures of neuronal
1408 maturation. *Cell reports methods* **4**, 100858 (2024).
1409 87. Andreatta, M. & Carmona, S. J. UCell: Robust and scalable single-cell gene signature scoring.
1410 *Comput. Struct. Biotechnol. J.* **19**, 3796–3798 (2021).
1411 88. Van de Sande, B. *et al.* A scalable SCENIC workflow for single-cell gene regulatory network
1412 analysis. *Nat. Protoc. 2020 157* **15**, 2247–2276 (2020).
1413 89. Wolf, F. A., Angerer, P. & Theis, F. J. SCANPY: Large-scale single-cell gene expression data
1414 analysis. *Genome Biol.* **19**, 15 (2018)

Figure 1:

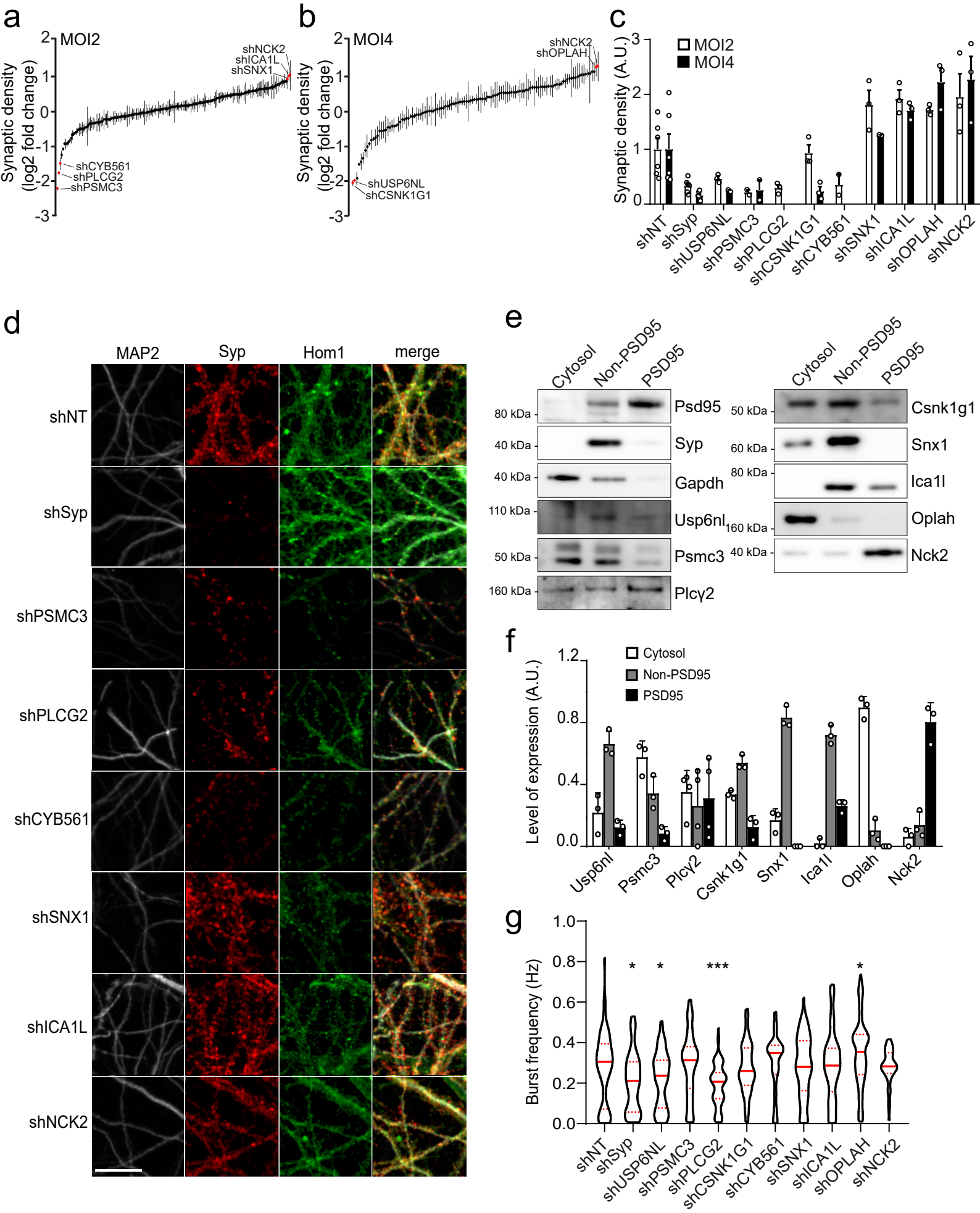
a
MOI2
Synaptic density (log2 fold change)
shNCK2
shICA1L
shSNX1
shCYB561
shPLCG2
shPSMC3
b
MOI4
shNCK2
shOPLAH
shUSP6NL
shCSNK1G1
c
MOI2
MOI4
Synaptic density (A.U.)
shNT
shSyp
shUSP6NL
shPSMC3
shPLCG2
shCSNK1G1
shCYB561
shSNX1
shICA1L
shOPLAH
shNCK2
d
MAP2
Syp
Hom1
merge
shNT
shSyp
shPSMC3
shPLCG2
shCYB561
shSNX1
shICA1L
shNCK2
e
Cytosol
Non-PSD95
PSD95
80 kDa
Psd95
40 kDa
Syp
40 kDa
Gapdh
110 kDa
Usp6nl
50 kDa
Psmc3
160 kDa
Plcγ2
50 kDa
Csnk1g1
60 kDa
Snx1
80 kDa
Ica1l
160 kDa
Oplah
40 kDa
Nck2
f
Cytosol
Non-PSD95
PSD95
Level of expression (A.U.)
Usp6nl
Psmc3
Plcγ2
Csnk1g1
Snx1
Ica1l
Oplah
Nck2
g
Burst frequency (Hz)
shNT
shSyp
shUSP6NL
shPSMC3
shPLCG2
shCSNK1G1
shCYB561
shSNX1
shICA1L
shOPLAH
shNCK2

Figure 2:

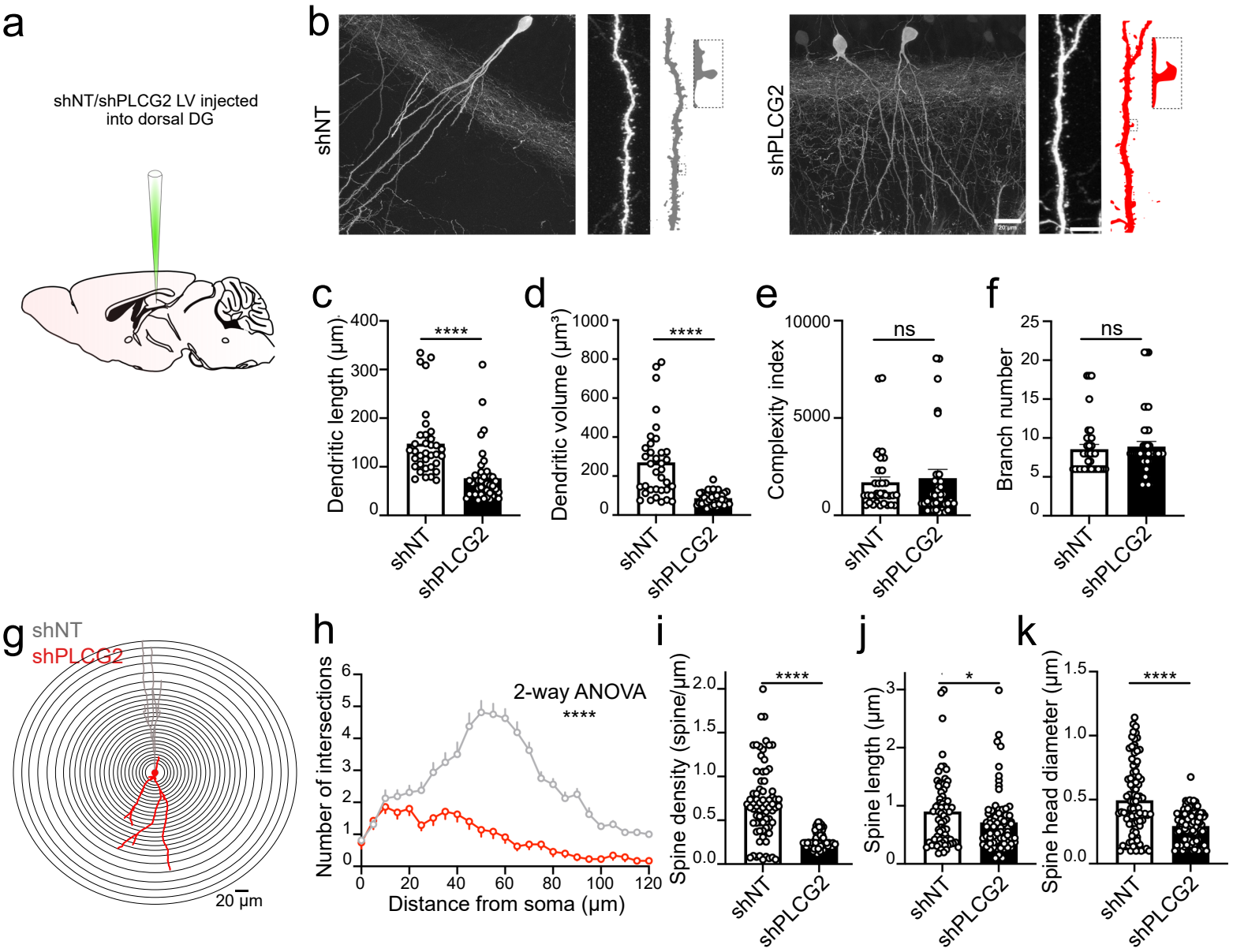
a
shNT/shPLCG2 LV injected into dorsal DG
b
shNT
shPLCG2
c
Dendritic length (µm)
****
shNT
shPLCG2
d
Dendritic volume (µm³)
****
e
Complexity index
ns
f
Branch number
ns
g
shNT
shPLCG2
20 µm
h
Number of intersections
2-way ANOVA
****
Distance from soma (µm)
i
Spine density (spine/µm)
****
j
Spine length (µm)
*
k
Spine head diameter (µm)
****

Figure 3:

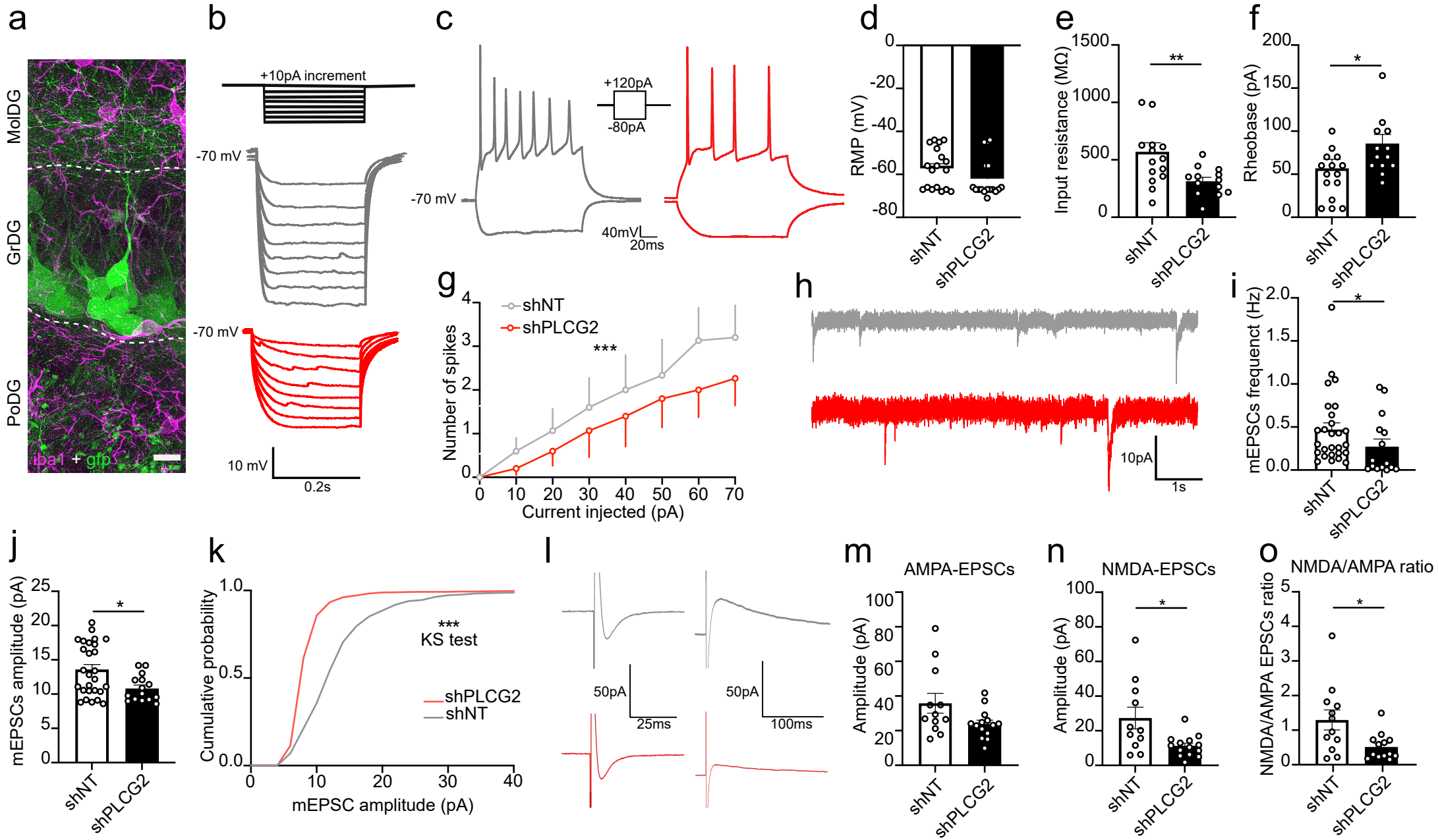
a
MolDG
GrDG
PoDG
iba1 + gfp
b
+10pA increment
-70 mV
-70 mV
10 mV
0.2s
c
+120pA
-80pA
-70 mV
40mV
20ms
d
RMP (mV)
shNT
shPLCG2
e
Input resistance (MΩ)
**
shNT
shPLCG2
f
Rheobase (pA)
*
shNT
shPLCG2
g
shNT
shPLCG2
***
Number of spikes
Current injected (pA)
h
10pA
1s
i
mEPSCs frequenct (Hz)
*
shNT
shPLCG2
j
mEPSCs amplitude (pA)
*
shNT
shPLCG2
k
Cumulative probability
***
KS test
shPLCG2
shNT
mEPSC amplitude (pA)
l
50pA
25ms
50pA
100ms
m
AMPA-EPSCs
Amplitude (pA)
shNT
shPLCG2
n
NMDA-EPSCs
Amplitude (pA)
*
shNT
shPLCG2
o
NMDA/AMPA ratio
NMDA/AMPA EPSCs ratio
*
shNT
shPLCG2

Figure 4:

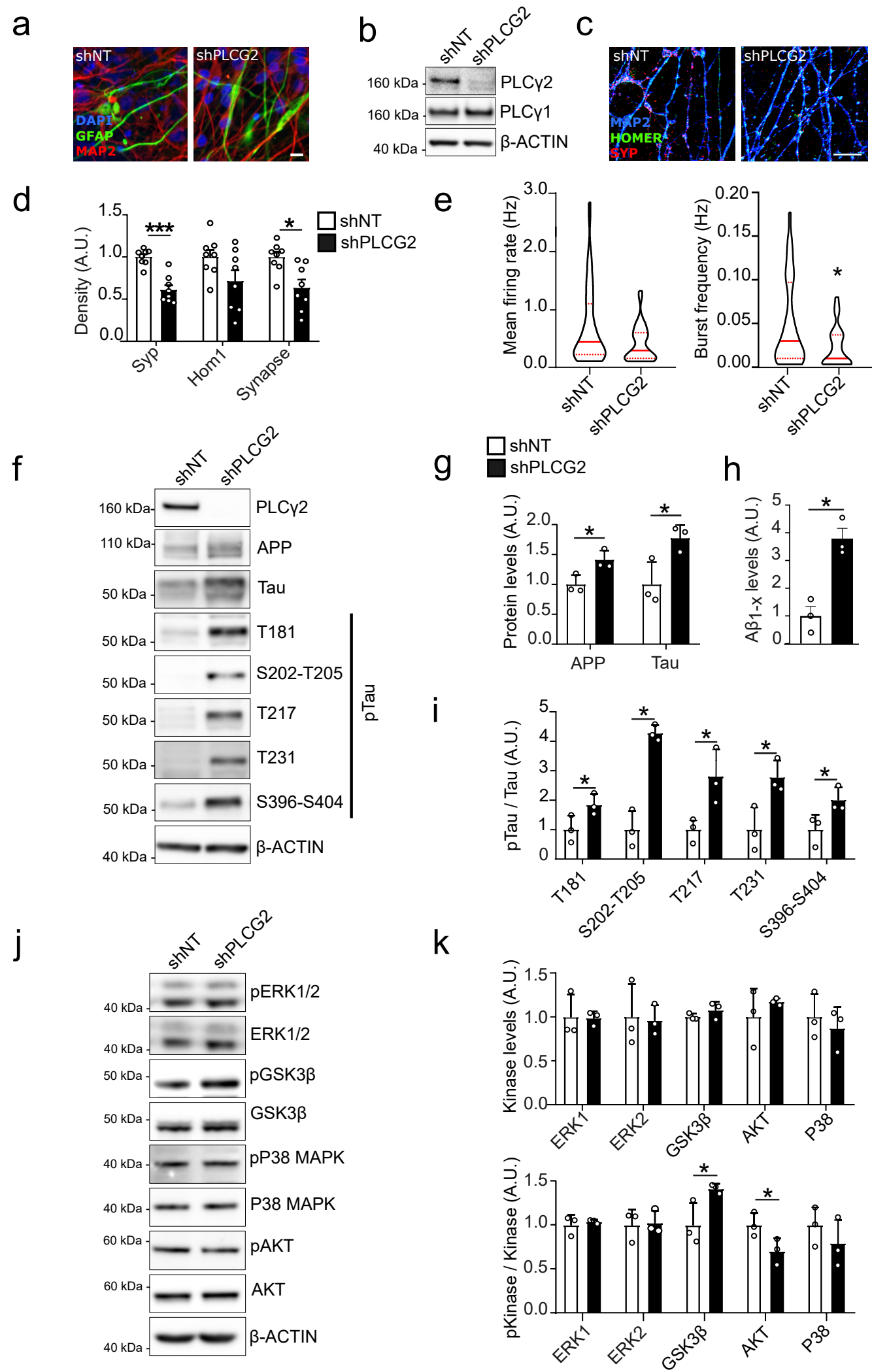
a
shNT
shPLCG2
DAPI
GFAP
MAP2
b
shNT
shPLCG2
160 kDa
PLCγ2
160 kDa
PLCγ1
40 kDa
β-ACTIN
c
shNT
shPLCG2
MAP2
HOMER
SYP
d
Density (A.U.)
1.5
1.0
0.5
0.0
***
*
shNT
shPLCG2
Syp
Hom1
Synapse
e
Mean firing rate (Hz)
3.0
2.0
1.0
0.0
shNT
shPLCG2
Burst frequency (Hz)
0.20
0.15
0.10
0.05
0.00
*
shNT
shPLCG2
f
shNT
shPLCG2
160 kDa
PLCγ2
110 kDa
APP
50 kDa
Tau
50 kDa
T181
50 kDa
S202-T205
50 kDa
T217
50 kDa
T231
50 kDa
S396-S404
40 kDa
β-ACTIN
pTau
g
shNT
shPLCG2
Protein levels (A.U.)
2.0
1.5
1.0
0.5
0.0
*
*
APP
Tau
h
Aβ1-x levels (A.U.)
5
4
3
2
1
0
*
i
pTau / Tau (A.U.)
5
4
3
2
1
0
*
*
*
*
*
T181
S202-T205
T217
T231
S396-S404
j
shNT
shPLCG2
40 kDa
pERK1/2
40 kDa
ERK1/2
50 kDa
pGSK3β
50 kDa
GSK3β
40 kDa
pP38 MAPK
40 kDa
P38 MAPK
60 kDa
pAKT
60 kDa
AKT
40 kDa
β-ACTIN
k
Kinase levels (A.U.)
1.5
1.0
0.5
0.0
ERK1
ERK2
GSK3β
AKT
P38
pKinase / Kinase (A.U.)
1.5
1.0
0.5
0.0
*
*
ERK1
ERK2
GSK3β
AKT
P38

Figure 5:

a

Study	Cases Carriers	Cases Non Carriers	Controls Carriers	Controls Non Carriers	OR	95%–CI
ADGEN	2	527	3	8707	11.05	[1.84; 66.29]
ADES	9	8732	1	8955	9.24	[1.17; 72.93]
	11	**9259**	**4**	**17662**		
Common effect model					**9.70**	**[1.97; 47.69]**
Random effects model					**10.23**	**[2.64; 39.62]**

Heterogeneity: $I^2 = 0\%$, $\tau^2 = 0$, $p = 0.90$

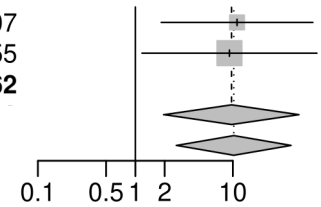

b

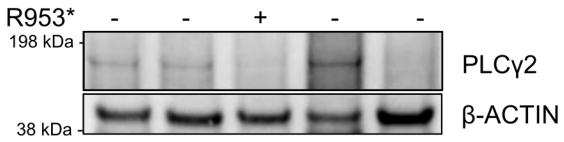

c

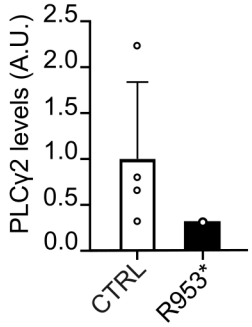

d

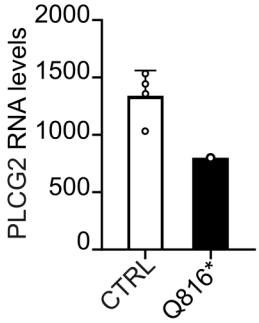

e

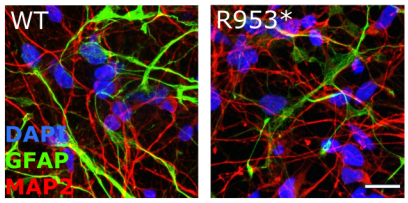

f

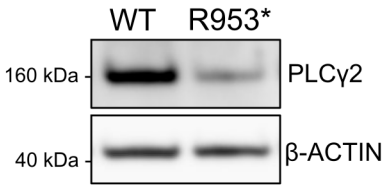

g

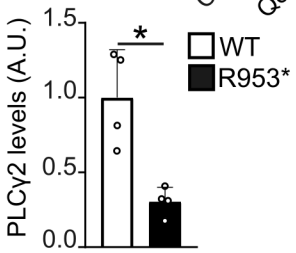

h

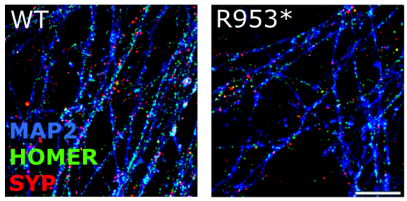

i

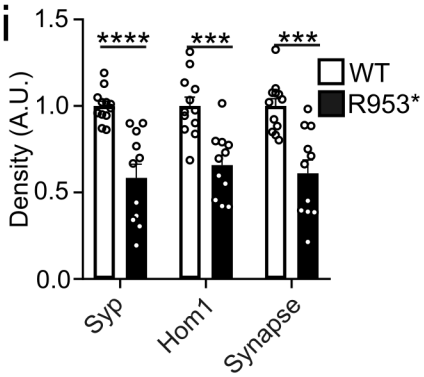

j

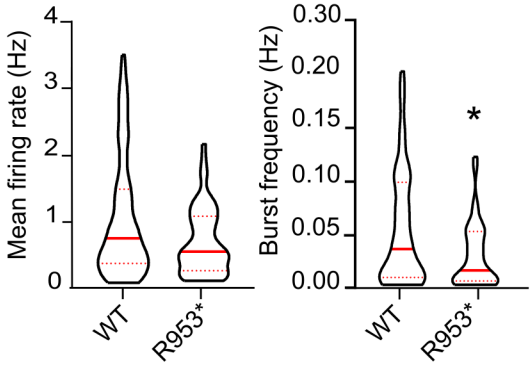

k

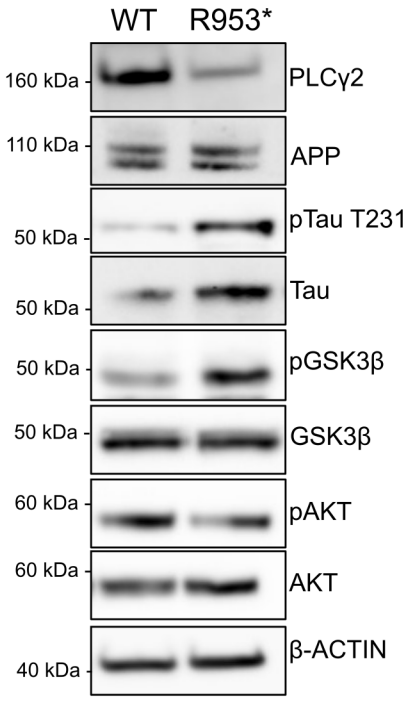

l

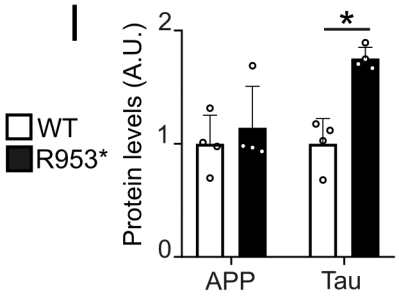

m

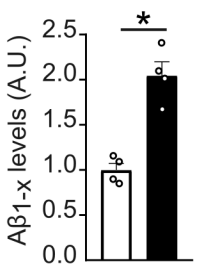

n

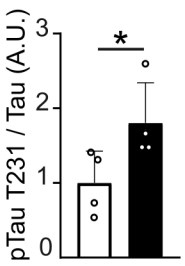

o

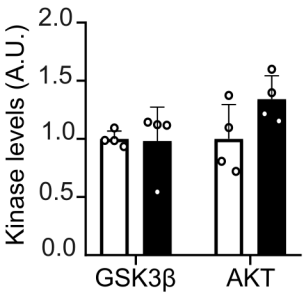

p

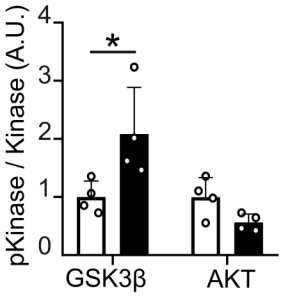

Figure 6:

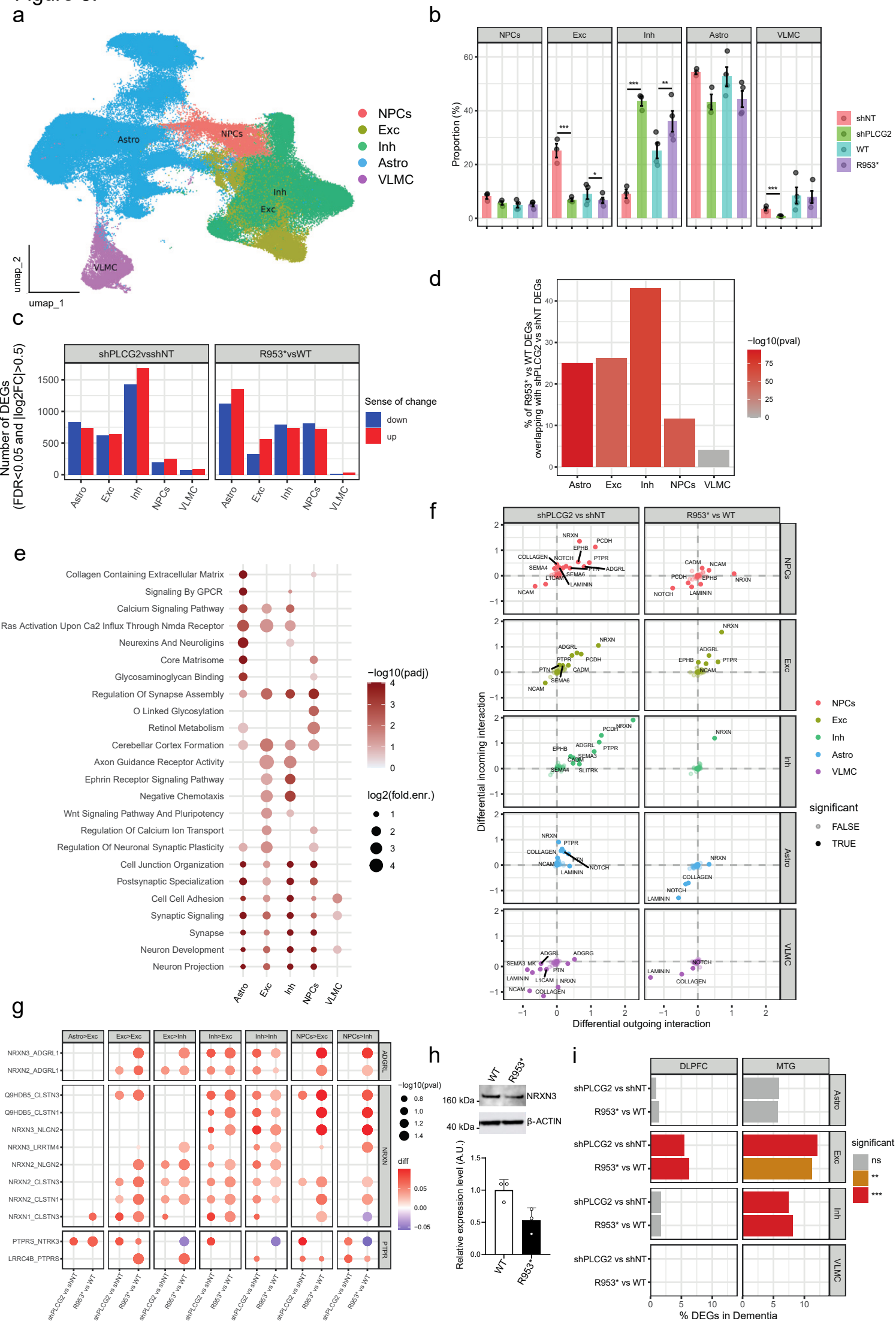
a
NPCs
Exc
Inh
Astro
VLMC
umap_1
umap_2
b
Proportion (%)
shNT
shPLCG2
WT
R953*
c
shPLCG2vsshNT
R953*vsWT
Number of DEGs (FDR<0.05 and |log2FC|>0.5)
Sense of change
down
up
d
% of R953* vs WT DEGs overlapping with shPLCG2 vs shNT DEGs
−log10(pval)
e
Collagen Containing Extracellular Matrix
Signaling By GPCR
Calcium Signaling Pathway
Ras Activation Upon Ca2 Influx Through Nmda Receptor
Neurexins And Neuroligins
Core Matrisome
Glycosaminoglycan Binding
Regulation Of Synapse Assembly
O Linked Glycosylation
Retinol Metabolism
Cerebellar Cortex Formation
Axon Guidance Receptor Activity
Ephrin Receptor Signaling Pathway
Negative Chemotaxis
Wnt Signaling Pathway And Pluripotency
Regulation Of Calcium Ion Transport
Regulation Of Neuronal Synaptic Plasticity
Cell Junction Organization
Postsynaptic Specialization
Cell Cell Adhesion
Synaptic Signaling
Synapse
Neuron Development
Neuron Projection
−log10(padj)
log2(fold.enr.)
f
shPLCG2 vs shNT
R953* vs WT
Differential incoming interaction
Differential outgoing interaction
significant
FALSE
TRUE
g
Astro>Exc
Exc>Exc
Exc>Inh
Inh>Exc
Inh>Inh
NPCs>Exc
NPCs>Inh
NRXN3_ADGRL1
NRXN2_ADGRL1
Q9HDB5_CLSTN3
Q9HDB5_CLSTN1
NRXN3_NLGN2
NRXN3_LRRTM4
NRXN2_NLGN2
NRXN2_CLSTN3
NRXN2_CLSTN1
NRXN1_CLSTN3
PTPRS_NTRK3
LRRC4B_PTPRS
−log10(pval)
diff
h
WT
R953*
160 kDa
NRXN3
40 kDa
β-ACTIN
Relative expression level (A.U.)
i
DLPFC
MTG
shPLCG2 vs shNT
R953* vs WT
significant
ns
**
***
% DEGs in Dementia
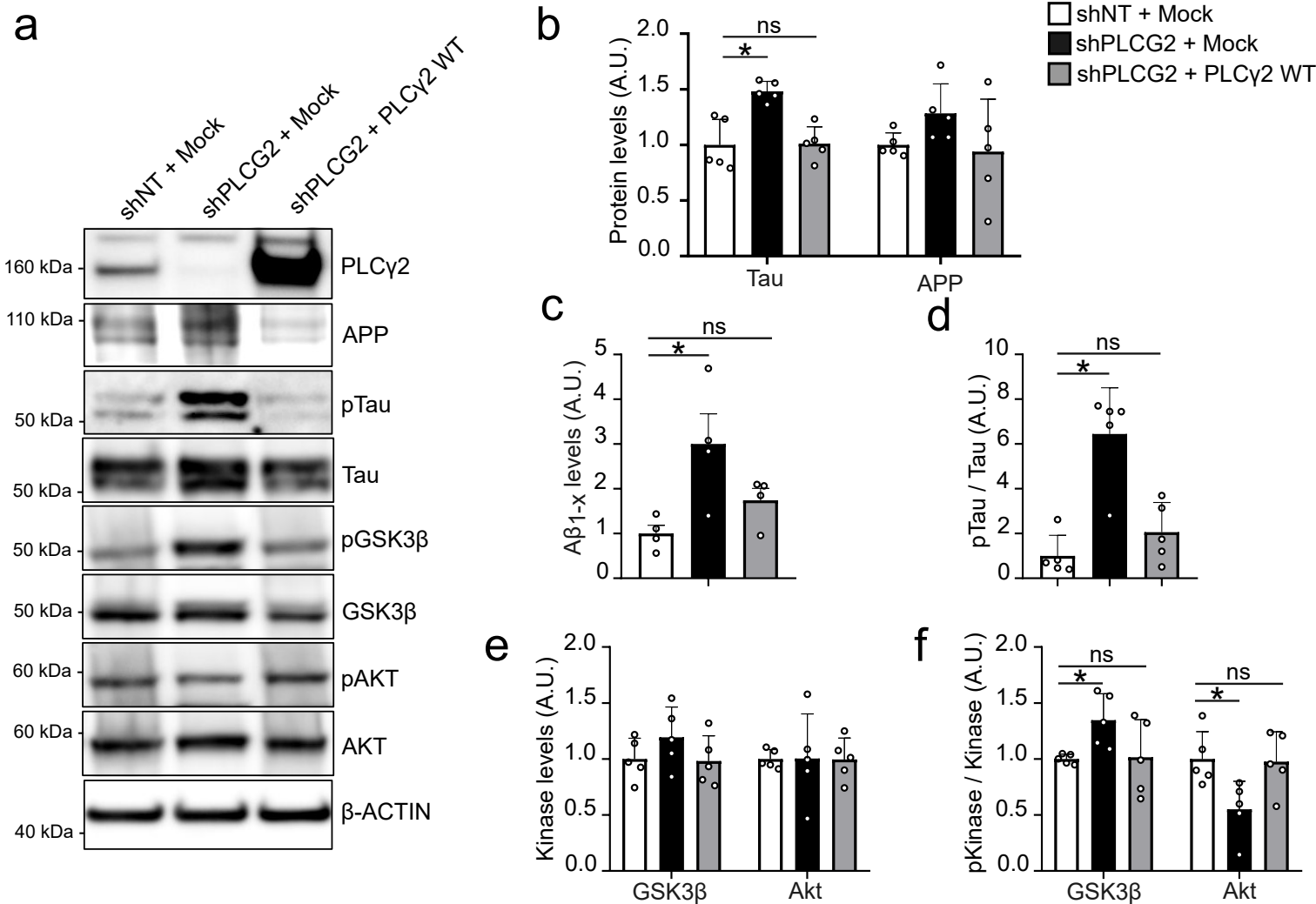
Extended figure 1: